Solid-state cathode heterogeneity impact on utilization and fracture dynamics

Se Hwan Park[1], Carlos Juarez Yescas[2], Kaustubh G. Naik[3], Yingjin Wang[4], Yuting Luo[2,5,6], Dhanya Puthusseri[1], Partick Kwon[2], Bairav S. Vishnugopi[3], Badri Shyam[7,] Heng Yang[7], John Cook[7] John Okasinki[8], Andrew Chaung[8], Xianghui Xiao[9], Julia R. Greer[4, 10], Partha P. Mukherjee[3], Beniamin Zahiri[2,5,6,*], Paul V. Braun[2,5,6,11*], Kelsey B. Hatzell[1,12*]

[1]Andlinger Center for Energy and the Environment, Princeton, NJ, USA

[2] Department of Materials Science and Engineering, University of Illinois Urbana-Champaign, Urbana, IL, USA

[3] School of Mechanical Engineering, Purdue University, West Lafayette, IN, United States

[4] Division of Engineering and Applied Science, California Institute of Technology, Pasadena, CA, United States

[5] Materials Research Laboratory, University of Illinois Urbana-Champaign, Urbana, IL, USA

[6] Beckman Institute for Advanced Science and Technology, University of Illinois Urbana–Champaign, Urbana, IL, USA

[7] Xerion Advanced Battery Corporation, Kettering, OH, USA.

[8] Advanced Photon Source, Argonne National Laboratory, Lemont, IL, USA.

[9] National Synchrotron Light Source II, Brookhaven National Laboratory, Upton, NY, USA.

[10] Kavli Nanoscience Institute, California Institute, California Institute of Technology, Pasadena, CA, United States

[11]Department of Chemistry, University of Illinois Urbana-Champaign, Urbana, IL, USA

[12] Department of Mechanical and Aerospace Engineering, Princeton, NJ, USA

*Kelsey.hatzell@princeton.edu, pbraun@illinois.edu, bzahiri@illinois.edu

Abstract

Structural heterogeneity in solid-state batteries can impact material utilization and fracture mechanisms. Dense crystallographically oriented lithium cobalt oxide cathodes serve as a model electrode system for exploring how density variability contributes to stress relief and build up during cycling. Real- and reciprocal-space *operando* and *ex-situ* synchrotron based experiments are utilized to understand structural changes across multiple length scales contribute to stress generation and fracture. Nanotomography uncovers a depth-dependent porosity variation in the pristine electrode and highlights preferential fracture in regions of lower porosity during delithiation. Energy-dispersive X-ray diffraction and 3D X-ray absorption near-edge spectroscopy (XANES) reveal the underutilization of cathode material in these regions. 3D XANES also confirms preferential delithiation near the sub-grain boundaries. Chemo-mechanical modeling coupled with site-specific mechanical characterization demonstrate how stress accumulation in dense regions of the electrode leads to fracture and underutilization of active material. Our findings reveal the importance of materials design to alleviate stress in small-volume changing cathodes.

Main

Solid-state batteries (SSBs) offer both high energy density and enhanced safety for next generation energy storage systems[1–3]. Maintaining contact between the solid ion conducting phase and solid active material phase is critical for achieving rate performance and suppressing a range of degradation modes[4,5]. Active material volume change occurs during lithiation and delithiation of the cathode and anode active material. The magnitude of volume change is often unequal between each electrode. Li metal anodes can experience 100% or infinite volume changes (reservoir-free)[5–9] and layered oxide cathodes can experience <3% volume changes[10]. Extensive efforts focus on how high-volume change anode materials can accelerate reaction heterogeneity, drive filament formation, and cause electrical shorting and fracture[4,11,12]. The impact of small volume changes in the cathode active material has drawn less attention and most studies focus on single particle dynamics in composite solid-state cathodes[4,13–15] Unraveling the relationship between structural heterogeneity and chemo-mechanics is critical for understanding degradation mechanisms and optimizing solid-state battery architectures for long cycle lifetime.

Composite solid-state cathodes combine a solid-state ion conductor with a cathode active material (Figure 1a). This composite structure is composed of a complex three-dimensional networks of solid-solid contact sites between the solid electrolyte phase and cathode active material phase. Structural heterogeneity exists across multiple length scales and can influence active material utilization and fracture progression. At the particle level polycrystalline active material consists of grains and at the electrode level porosity, contact area, and variable composition can all influence electrochemical and degradation processes. Heterogeneity in cathodes can drive interfacial delamination, side reaction, and non-uniform ion transport[4,13,14]. It is challenging to directly interrogate how cathode structural heterogeneity influences utilization and fracture progression. Consequently, a suitable model system should be devised to minimize the complex three-dimensional solid-solid interfaces to intensively explore the impact of electrode's structural heterogeneity. Also, due to the intricate coupling between electrochemical reaction and chemo-mechanical interactions, conventional electrochemical and *ex-situ* materials characterization techniques have limitations in fully elucidating the effects of structural heterogeneity.

To minimize effects born from cathode active material delamination from the solid electrolyte in a composite cathode, we studied a dense electroplated and crystallographically oriented lithium cobalt oxide (LCO). These electroplated cathodes have (003) basal planes nearly perpendicular to the current collector to facilitates rapid Li ion diffusion across the thickness of the electrode. Using crystalloraphically oriented cathodes eliminates the need for a solid ion conducting phases in the cathode and enable direct investigation of chemo-mechanical transformation in the cathode active materials phase in a solid-state battery (Figure 1b-d). [16] We combine multiple techniques, including *operando* and *ex-situ* synchrotron-based characterizations to uncover the relationship between structural heterogeneity and reaction dynamics. *Operando* energy dispersive X-ray diffraction (EDXRD) and *ex-situ* 3D XANES identify spatially resolved electrochemical reaction heterogeneity and X-ray nanotomography probes nano-scale morphological transformations and fracture dynamics. The results demonstrates that preferential fracture and loss of accessible capacity originates from highly dense region of the cathode active material. Combining real and reciprocal-space techniques with electrochemical-transport and chemo-mechanical modeling unravels the role intrinsic porosity plays on stress relief. Local porosity variability can result in local changes to fracture toughness. Exquisite control over pores in solid-state cathodes can potentially aid in suppressing fracture in thick cathodes.

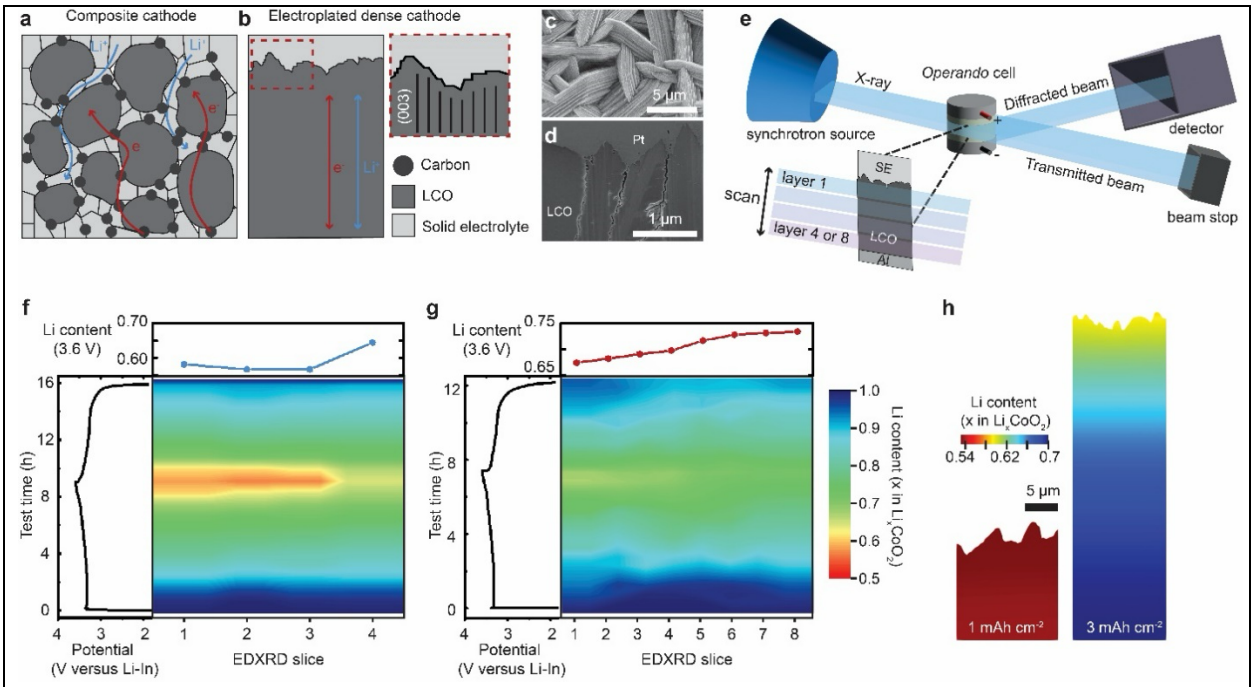

Figure 1| **(a)** Depiction of a composite solid-state cathode with complex 3-dimensional solid-solid contacts and (**b**) electroplated dense cathode. **c, d,** SEM images of electroplated dense LCO showing the (**c**) top view and (**d**) cross-sectional view. **e**, Schematic representation of the operando EDXRD setup. **f,g,** Galvanostatic charge and discharge voltage profiles and corresponding local Li content (x in Li_xCoO_2) for (**f**) 1 and (**g**) 3 mAh cm^{-2} LCO. Graphs above the contour map represent local Li content variation through the depth after charge to 3.6 V with current density of 0.1 C (0.1 and 0.3 mA cm^{-2} for 1 and 3 mAh cm^{-2} LCO, respectively). (**h**) Local Li content maps after charge to 3.6 V obtained by electrochemical-transport modeling.

Reaction heterogeneity throughout the thickness of textured LCO

Operando EDXRD can spatially resolve *d-spacing* changes through the thickness of a cathode with a spatial resolution up to 5 µm[16,17]. Monitoring the d-spacing during galvanostatic cycling experiments sheds light on active material utilization in thick monolithic electrode materials (Figure 1e). This enables tracking dynamics from the cathode-solid electrolyte interface (Layer 1) to current collector-cathode interface (Layer 4 or 8, Figure 1e). The dense electroplated cathodes are absent of any binder and additive and thus the thickness of the cathode scales with the capacity of 1 mAh cm^{-2} (17 ± 3 µm) and 3 mAh cm^{-2} (50 ± 5 µm). It is possible to monitor 4 distinct locations across the thickness of 1 mAh cm^{-2} cathode and 8 distinct locations across the 3 mAh cm^{-2} cathode due to the beamline resolution (~5 µm). This technique can directly monitor the degree of lithiation or delithiation during charging (decrease in lithium content) and discharging (increase in lithium content). Changes in the unit cell volume are used to estimate the Li content[18]. The unit cell volume changes are greatest in the region near the solid electrolyte interface (Layers 1-3) for the 1 mAh cm^{-2} (17 µm) LCO cathode. The unit cell volume increases by ~ 2% (Figure S1a) during the first 8 hours of charging. The rate of volume increase decreases (0.1%) between 8 and 9 hours of charging. These unit cell volume changes are consistent with previous reports[10,19,20]. The degree of lithiation and delithiation is uniform across the thickness of the 1 mAh cm^{-2} (17 µm) LCO cathode and demonstrates only minor underutilization in the region adjacent to the current collector (layer 4) (Figure 1f). The 1 mAh

cm^{-2} (17 µm) LCO cathode delithiates to Li contents around 0.57-0.58 in layers 1-3 (x in Li_xCoO_2). Incomplete delithiation around the current collector (layer 4) results in Li content of 0.64. As seen in earlier studies investigating reaction dynamics in solid-state sulfur and NMC cathode through neutron imaging and EDXRD, insufficient effective ion transport leads to local reaction rate heterogeneity within solid-state battery cathodes[21,22]. Limited ion transport makes the reaction front propagate from the solid electrolyte side to current collector. This reaction heterogeneity induces a Li concentration gradient along the thickness of the electrode. When ion transport is sufficient with respect to the applied current, reaction can be homogeneous within the electrode enabling the uniform Li concentration during the reaction.

The lithium content is relatively uniform across the thickness of the 1 mAh cm^{-2} LCO electrode during charge and discharge (Figure 1g). The high capacity, thick LCO cathode 3 mAh cm^{-2} (~50µm) demonstrates a greater Li content gradients throughout the cathode thickness (Figure 1f). After the first charging period, the cathode material near the solid electrolyte (layer 1) has the lowest Li contents of 0.64, while the cathode material near the current collector (layer 8) has the highest Li contents of 0.73. The 3 mAh cm^{-2} LCO cathode experiences a gradient in delithiation moving through the thickness of the cathode from the solid electrolyte to the current collector region which is due to the limitation in Li diffusion within the cathode[21,22]. Incomplete delithiation of this cathode leads to a low cell level capacity.

A coupled electrochemical-transport model sheds light on reaction and transport interactions in the electroplated LCO cathodes (Figure 1h, S2). All details regarding the mathematical formulation and associated parameters are provided in the Method section. The model solves for the ionic transport in the solid electrolyte, reaction kinetics at LCO|solid electrolyte interface and solid-state lithium diffusion with the LCO cathode. 2D image slices of 1 and 3 mAh cm^{-2} LCO obtained through synchrotron nanotomography provide a surface profile of the electrodes for modeling (Figure S3). 1 mAh cm^{-2} LCO demonstrates uniform Li contents across the entire cathode at the end of charging. In contrast, significant Li concentration gradients develop in 3 mAh cm^{-2} LCO. The higher areal current density and longer Li diffusion pathways for Li in 3 mAh cm^{-2} LCO induce transport limitations, leading to large Li concentration gradients [23,24]. While the model correctly captures the overall trend in the diffusion behavior and delithiation dynamics, the EDXRD results reveal some distinct characteristics of underutilization in the layer adjacent to the current collector (layer 4). Underutilization of certain regions of the cathode is a result of porosity variation throughout the thickness of the cathodes and is investigated in the next section.

Microstructure-dependent reaction heterogeneity in LCO electrode

Three-dimensional X-ray absorption near edge spectroscopy (3D XANES) enables simultaneous visualization of lithiation gradients and LCO cathode nanostructural features (morphological heterogeneities). Co K-edge XANES spectra of each voxel are collected via assessing the X-ray absorption of the sample under different energy levels (Figure 2a). White line energy which exhibits the highest X-ray absorption intensity is an indicator of increase in Co oxidation state (i.e., the delithiation state)[25]. Higher energies represent a high degree of delithiation and lower energies represent a low degree of delithiation. 3D XANES over the entire thickness of the charged 1 mAh cm^{-2} electrode demonstrates electrode thickness-dependent delithiation and preferential delithiation along core region of grain (Figure 2b). 3D XANES also confirms the uniform utilization throughout the thickness of LCO electrode but underutilization near the current collector which is consistent with EDXRD results. The white line energy is uniform in bulk region >3 µm from the current collector. Energies range from 7730.5 to 7730.6 eV and decrease progressively near the current collector to 7730.2 eV (Figure 2c). Sliced images from 3-D tomographys confirms the presence of a lower white line energy region near the current collector side of LCO (white dashed box in Figure 2e).

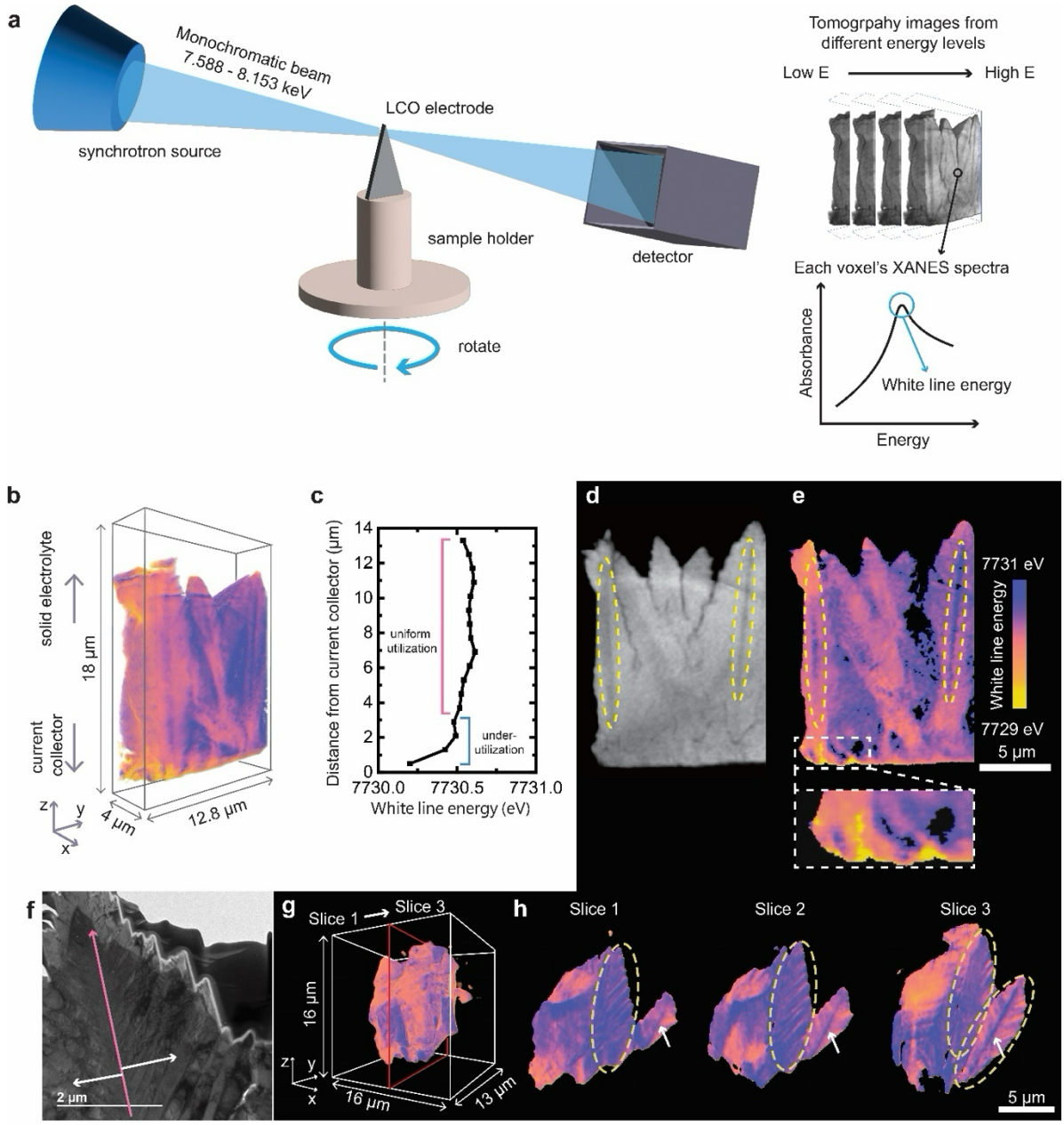

Figure 2 | 3D XANES mapping of LCO after charge.
a. Schematic illustration of ex-situ 3D XANES setup. **b**, 3D Co white line energy distribution for charged LCO. **c**, Variation of white line energy as a function of distance from the current collector. White line energy is the average white line energy of each XY plane with thickness of 0.8 µm. **d**, Reconstructed YZ plane 2D tomography image slice. **e**, Corresponding white line energy distribution. **f**, TEM image of LCO prepared via FIB. **g**, 3D white line energy distribution of LCO particle delaminated from the electrode **h**, 2D image slices of the YZ plane.

Transmission electron microscopy (TEM) analysis on cross section of the LCO shows microstructure where branch-like sub-grains extend on both side from central core (Figure 2f). We speculate a screw dislocation growth during electroplating, where the central core (darker region) grows in <110> direction (pink arrow in Figure 2f) and grain grows in <003> direction (white arrow in Figure 2f)[26], may create the observed microstructure[27]. The growth directions were confirmed through high resolution TEM analysis[26]. The <110> growth direction provides fast Li ion diffusion pathways[26,28]. 3D XANES on the entire thickness of LCO confirms the preferential delithiation near the central cores which traverse the entire thickness of the electrode from the solid electrolyte to the current collector (Figure 2d,e, yellow dashed). Internal grains demonstrate lower levels of delithiation. Fast Li diffusion following the <110> direction causes the preferential delithiation. 3D XANES on a particle delaminated from the charged LCO electrode reveals more pronounced preferential delithiation following the sub-grain boundaries than 3D XANES on entire thickness of electrode (Figure 2g, h). This clearer observation might be due to the smaller sample size. The particle is composed of a few single crystal grains (Figure S4). The preferential delithiation following the central core crossing the grain is apparent (white arrows in Figure 2h). Also, the particle has more delithiated branch-like regions which most likely correspond to sub-grain boundaries (yellow dashed circle in Figure 2h). These preferential delithiation features might be the result of the enhanced Li ion diffusion at sub-grain boundaries[29,30].

Morphological heterogeneity and structure changes of LCO

Ex-situ synchrotron X-ray nanotomography of a pristine, charged and discharged 1 mAh cm^{-2} LCO electrode reveals the nanostructural origin of the reaction heterogeneity. Intensity contrast between the LCO cathode and void allows for clear segmentation within electrode (Figure 3a, b). The rough surface of electrode (in contact with the solid electrolyte) and pores extending from the surface toward current collector are consistent with the FIB-SEM (Figure 1c, d) and with other electroplated lithium and sodium transition metal oxides [26,31–33]. The pristine electrode demonstrates structural heterogeneity throughout the thickness of the electrodes (Figure 3c, d, S5).

Grains and pores extend across the entire thickness of the cathode. The region near the current collector demonstrates a higher density (lower porosity) than the rest of the electrode and the presence of isolated pores (< 1 µm). 2D image slices of reconstructed tomography also reveal networks of connected pores that extend from the electrode surface to around 2 µm away from the current collector (Figure S6). Other regions in pristine LCO also exhibit similar trends (Figure S7). The porosity of the electrode is approximately 6.5% near the surface and 1% in the 2 µm region near the current collector. The electrode microstructure undergoes changes during delithiation (Figure 3e,f). The electrode material near the current collector shows porosity increase from 1% to around 4.5% (Figure 3f, S8-10). The electrode microstructure in the region away from the current collector demonstrates less of a change. The porosity in the bulk region (>5 µm from the current collector) only decreased by about 1% after delithiation. The porosity increases by about 1% across all electrode regions after lithiation to 1.9V (Figure 3g,h). Charging (delithiation) and discharging (lithiation) dynamics result in irreversible pore generation in the electrode region adjacent to the current collector (Figure S11-13).

The reversible volume expansion and contraction of LCO unit cell during delithiation and lithiation (~ 2%)[10] can drive fracture dynamics which create the void or pore region. The relatively high porosity of the bulk region can accommodate volume changes and alleviate stress accumulation. Therefore, the bulk region demonstrates reversible porosity changes during the initial cycle. However, the absence of enough pores near the current collector leads to stress buildup during the charging, which can cause fracture and increase porosity. The fractures near the current collector side interrupt the Li diffusion pathway and limit the full active material utilization at this region as observed through *operando* EDXRD analysis (Figure 1e)[14,34].

The 3 mAh cm^{-2} LCO also exhibits similar structural heterogeneity with a higher density of active material at the current collector (lower porosity) and a lower density (higher porosity) through the electrode thickness. The region near the current collector (<10 µm from the current collector) is almost perfectly dense with less than 1% calculated porosity (Figure S14). The porosity gradually increases, to around 10.6% in the region 40 µm from the current collector. Charging the cathode results in an increase in porosity near the current collector like the thin LCO cathodes (1 mAh cm^{-2} LCO) (Figure S15). However, the magnitude of the porosity changes are greater for the 3 mAh cm^{-2} LCO cathode. The porosity near the current collector increases from below 1% to around 4.5% for the 1 mAh cm^{-2} LCO and to around 8.5% for the 3 mAh cm^{-2} LCO. Significant fractures with thicknesses exceeding 2 µm traverse the entire electrode after charging (Figure S16). The 3 mAh cm^{-2} LCO cathodes have lower active material utilization, lower volume expansion, and more severe fracturing than the 1 mAh cm^{-2} LCO cathodes. The differences in fracture propagation may be linked with the dense region near the current collector. The highly dense region near the current collector is around 2 and 10 µm for 1 and 3 mAh cm^{-2} LCO, respectively. Thick dense regions impede stress relief toward the surface side. Consequently, greater stress buildup in dense areas leads to more significant fracturing.

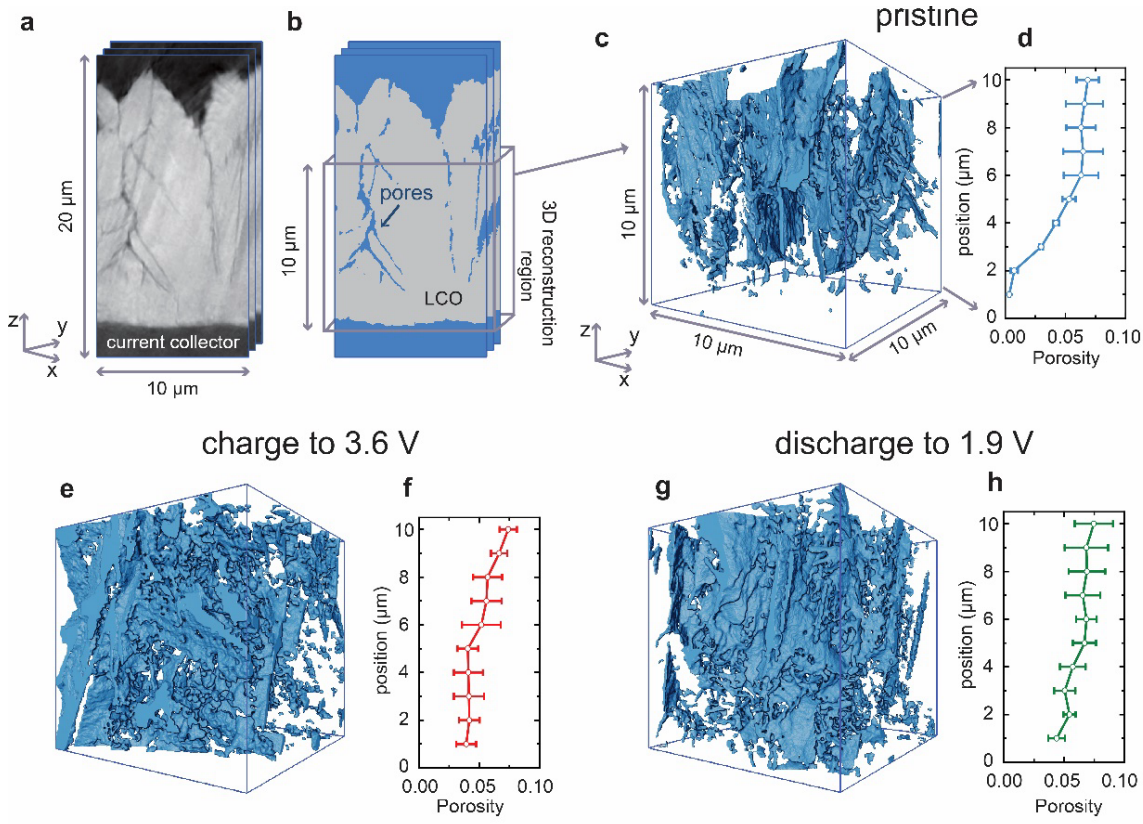

Figure 3 | Structural heterogeneity analysis using synchrotron nanotomography.
Reconstructed 2D image slice of LCO electrode. **b**. Segmented 2D image slice of corresponding LCO. 3D reconstruction of pores was carried out for the electrode region from the Al current collector surface to a distance of 10 µm. **c**,**e**,**g**, Reconstructed 3D image of pores in the LCO electrode for (**c**) pristine, (**e**) charged to 3.6 V, and (**g**) discharged to 1.9 V. **d**,**f**,**h**, Porosity variation along the z-axis in LCO electrode (**d**) pristine, (**f**) charged, and (**h**) discharged LCO, with position 0 at the current collector surface.

Fracture toughness variability

Fracture toughness serves as a key material parameter for predicting crack stability and its propensity for propagation under stress. To understand how structural heterogeneity contributes to the mechanical property landscape, we performed nanoindentations on a cross-sectional LCO sample using a Berkovich indenter tip in a G200 nanoindenter (Agilent, Inc.) at four different locations across the electrode thickness (Figure 4a). Figure 4b reveals the residual indentation marks, which radial and lateral cracks emanating from the sharp corners that serve as sufficiently high stress concentrations for crack initiation (Figure 4b). We find that in its pristine state, the electrode displays a similar fracture toughness along its height, with the average toughness ranging from 0.73 to 0.75 MPa $m^{0.5}$, with the layer adjacent to the current collector having a higher fracture toughness of 1.00 ± 0.16 MPa $m^{0.5}$ (Figure 4c). The lower porosity near the current collector can explain the greater fracture toughness in that location compared to the rest of the electrode (Figure 3d)[35,36].

After delithiation to 3.6 V vs. LiIn (4.2 V vs. Li), fracture toughness around the current collector decreases to 0.8 MPa $m^{0.5}$, a 20% decrease compared to pristine LCO (Figure 4d). The fracture toughnesses measured along the electrode cross-section, at distances of 5, 9, and 13 µm from the current collector, are tightly distributed in the range of 0.74 to 0.70 MPa $m^{0.5}$, a 5.6 % decrease from the pristine LCO. Studies of Li transition metal oxides have observed a similar reduction in fracture toughness near the current collector and attributed it to charging-induced Li depletion, residual stress, and micro-crack generation[37,38]. The bulk region (layer 1-3 in Figure 1f and 5-13 µm in Figure 4c,d) has the greatest delithiation and active material utilization (Figure 1f) and the smallest change in fracture toughness (Figure 4c, d). Our results indicate that the material in the vicinity of the current collector experiences the largest change in fracture toughness of 20% and lowest active material utilization (minimal delithiation), which suggests that Li depletion is unlikely to be the root cause for the fracture toughness variation. Most probably, it is the creation of pores, nano-cracks, and voids that drive fracture toughness reduction. This is consistent with our observation that the fracture toughness becomes more uniform throughout the remaining thickness of the LCO electrode, following the porosity gradient (Figure 3e, f).

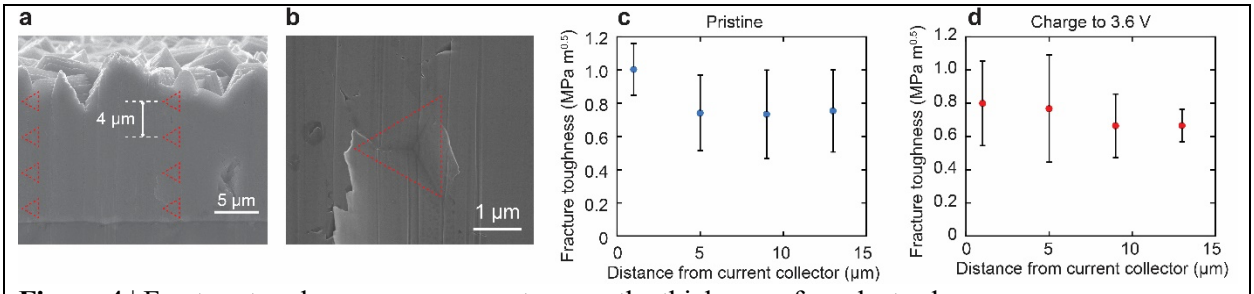

Figure 4 | Fracture toughness measurement across the thickness of an electrode.
SEM images of **a**, the LCO electrode cross-section after nanoindentation. The residual indents are marked as red triangles. **b**, a typical individual indent mark. **c, d**, Fracture toughness, calculated from displacement bursts (pop-ins) in load-displacement data corresponding with crack formation, as function of distance away from current collector for (**c**) pristine and (**d**) charged LCO.

Pore stability prediction through mechanics modeling

The electrochemical-transport model developed in this work is coupled with the mechanics model to understand chemo-mechanical coupling in the LCO electrodes. Here, the time-dependent concentration field obtained using the electrochemical transport model is systematically fed into the mechanics model to determine the stress evolution within the system. The details about the chemo-mechanical modeling are provided in the Method section. Segmented 2D images provide structural information for modeling. In 2D images, pores that are interconnected frequently appear as separate entities. Thus, we selected the 2D image slice that demonstrates high pore connectivity as the representative image for modeling (Figure 5a). Furthermore, to assess the stress applied to isolated pores near the current collector side, we integrate pores into the image slice at 1 μm apart from the current collector. Given the electrode's crystal orientation with (003) basal planes mostly perpendicular to the current collector, anisotropic expansion of LCO parallel to the current collector was assumed in the model.

As LCO delithiates, the accompanied volume change significantly affects the stress dynamics resulting in both compressive and tensile stresses (Figure 5b-d). The electrode experiences high compressive stress (~10 GPa) near the current collector and low stress (~1GPa) at the solid electrolyte-cathode interface (Y>4 μm) when charged for 8 hours when the volume expansion is maximum (Figure S1a). Pores in the electrode can accommodate the LCO volume expansion and mitigate stress accumulation. The relatively high porosity (~6.5%) in the bulk region (Y>4 μm) can accommodate LCO volume expansion, thereby reducing stress accumulation. Whereas lack of pores near the current collector (~1%) results in significant compressive stress accumulation.

To elucidate pore stability under these stress circumstances, we closely observe the stress locally applied to pore tips. Although compressive stress predominates in most regions of the electrode, pore tips experience tensile stresses and their magnitudes increase with the charging time (Figure 5b-d). These tensile stress hotspots can potentially lead to crack onset and propagation within the electrode. Three representative pores located at regions marked as A, B, and C (Figure 5d) exhibits stark difference in stress applied on pore tips (Figure 5e). Both pore tips located near the current collector (region A,B) experience a high tensile stress over 2 GPa. In contrast, the pore tip located 6 μm from the current collector (region C) experiences much lower tensile stress (<0.1 GPa). The comparison between maximum tensile stress at each pore tip (as marked in Figure 5a) and the corresponding limiting stress required for the pore opening can predict the pore stability during the initial charging process (Figure 5f). The following equation calculates the limiting stress:[39]

$$\sigma_f = \frac{1}{\gamma\sqrt{\pi/2}}\frac{K_{Ic}}{\sqrt{a}} \quad (1)$$

Here, K_{Ic} is the measured fracture toughness of LCO at a pristine state (Figure 4c) and a is the length of crack estimated from the 2D image slice. γ is a geometric correction factor that depends on the geometry of the crack and loading conditions. γ value is calculated based on the height of the electrode and pore length.[40] Pore tips near the current collector (Y<4 μm) experience tensile stress greater than the limiting stress, leading to pore opening. On the other hand, most pore tips located near to the solid electrolyte (Y>4 μm) experience stress less than limiting stress, preventing pore growth during charging. Also, the comparison with limiting stress calculated based on the fracture toughness of charged LCO exhibits the same results (Figure S17). Consequently, the fracture in the regions near the current collector leads to an

increase in the porosity, which in turn impedes effective Li ion diffusion and limits active material utilization. Conversely, the rest of the electrode can be fully utilized, exhibiting reversible porosity changes. Overall, this pore stability prediction through chemo-mechanical modeling highlights the importance of morphological heterogeneity in governing stress distribution, fracture dynamics, and concomitant transport limitations within the LCO electrode.

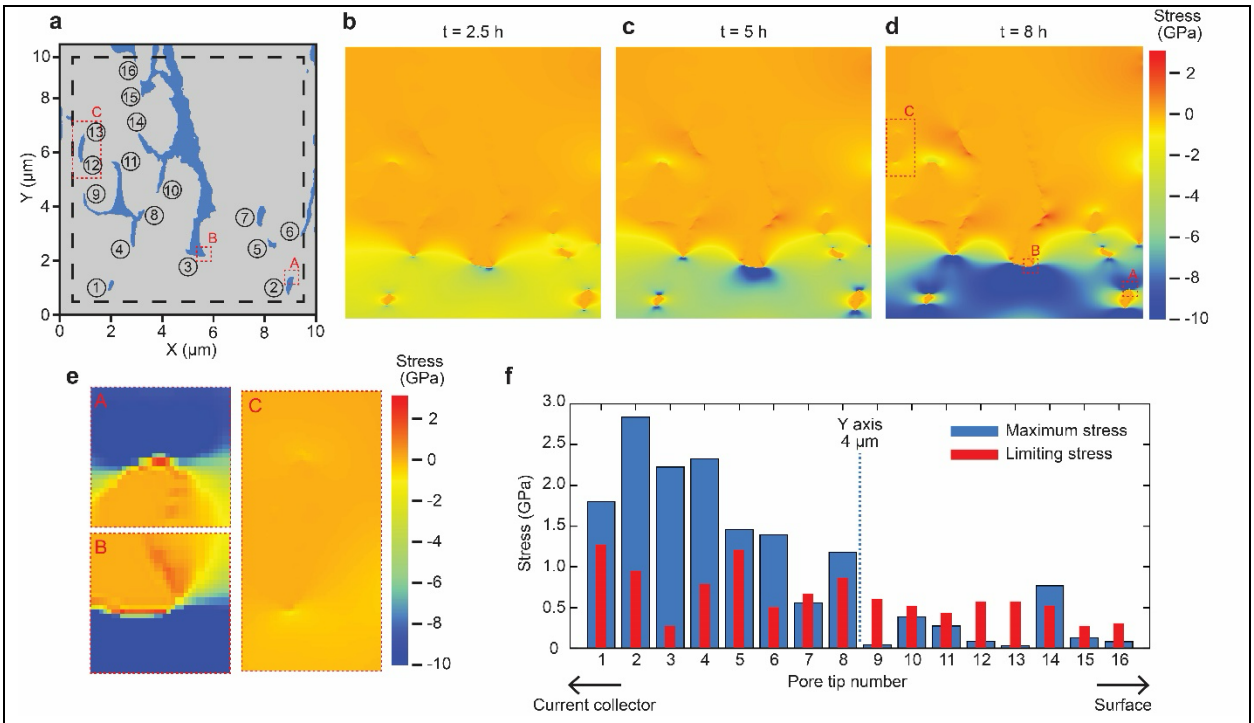

Figure 5 | Analysis of crack propagation in LCO electrode via chemo-mechanical modeling. **a**. Segmented 2D image slice of the pristine LCO electrode for stress modeling. The y-axis position 0 represents the current collector surface **b-d**. Corresponding stress distribution maps during charging at a current density of 0.1 C. Stress distribution maps are presented for the area delineated by a dashed black box in **a**. Positive and negative values indicate tensile and compressive stress, respectively. **c**, Magnified views of stress map in selected regions (marked as a dashed red box in **a** and **d**). **f**, Comparison of the maximum stress applied at each pore tip marked in **a** and corresponding limiting stress for crack growth.

Conclusions

Using electroplated and crystallographically textured LCO, we show the impact of morphological heterogeneity on active material utilization and chemo-mechanical interactions within an electrode which drive fracture. The absence of solid electrolyte within the electrode enables us to exclusively focus on the interaction originated from the morphological heterogeneity. *Operando* EDXRD and *ex-situ* 3D XANES analysis provide spatially resolved reaction heterogeneity both in entire electrode and single particle scale. EDXRD reveals variation throughout the electrode depth. 3D XANES confirms the EDXRD results of underutilization near the current collector in 1 mAh cm^{-2} LCO and also detects preferential delithiation along sub-grain boundaries. Both 1 and 3 mAh cm^{-2} LCO exhibits reaction heterogeneity but demonstrate pronounced difference. The Li contents gradient through the entire thickness of electrode in charged 3 mAh cm^{-2} LCO is attributed primarily to Li diffusion limitation within the electrode. In contrast, the limited charging solely near the current collector in 1 mAh cm^{-2} LCO originated from the morphological heterogeneity.

The depth-dependent structural heterogeneity and the morphology changes during the reaction are characterized by *ex-situ* synchrotron X-ray nanotomography. Electrodes exhibit high density near the current collector with less than 1% porosity, transitioning to higher porosity away from the current collector. The pores within the electrode function to accommodate the volume expansion of the LCO unit cell during charging. The lower porosity near the current collector leads to stress accumulation, resulting in fractures, whereas the relatively higher porosity in the rest of the electrode alleviates stress. Consequently, the current collector side suffers irreversible porosity increases, while all the other electrode regions exhibit reversible porosity changes which originated from the volume change of the LCO unit cell. Fractures near the current collector impede facile Li diffusion and limit the full utilization. This heterogeneous fracture mechanism is confirmed by combining fracture toughness measurement and chemo-mechanical modeling. Higher tensile stresses at the pore tips near the current collector lead to pore opening. These results extend our fundamental understanding of the effects of structural heterogeneity on mechano-electrochemical reactions and illuminate strategies to mitigate stress-induced fractures in designing electrode architecture.

Methods

1. Chemical and materials

Electroplated faceted LCO electrodes with two different loadings (1 and 3 mAh cm^{-2}) were supplied by Xerion Advanced Battery Corp (Kettering, Ohio). The electrodes were fabricated according to the process detailed in a previous study[32]. The electroplating bath was formulated by blending KOH and LiOH in a 5:1 weight ratio within an Ar-filled glove box and then heated to 260 °C to achieve a transparent molten salt mixture. Subsequently, 2 wt% CoO was added, resulting in a blue solution from the $Co(OH)_4^{2-}$ complex. A Co wire was used for the reference electrode, a Ni plate acted as the counter electrode, and Al foil was employed as the working electrode and used as a current collector for the electrodeposition. The mass loading corresponding to 1 and 3 mAh cm^{-2} are approximately 7.8 and 23.4 mg cm^{-2}, respectively.

Li_6PS_5Cl (LPSCl) solid electrolyte powder was purchased from NEI corporation (Somerset, New Jersey) and used as received. Li_3InCl_6 (LIC) and Li_3YCl_6 (LYC) were synthesized via mechano-chemical solid-state method according to the process described in an earlier study[26]. Lithium chloride (LiCl, from Sigma Aldrich) was combined and ground by hand with either yttrium chloride (YCl_3, from Alfa Aesar) to create a LYC blend or indium chloride (InCl3, from Alfa Aesar) for a LIC blend, following the molar ratio. During the manual grinding of LYC, an additional 10 wt% of YCl_3 or $InCl_3$ was included to compensate for any material lost through adherence to the milling equipment. The synthesis of the final solid electrolyte was carried out using a high-energy ball mill (SPEX 8000 Mixer/Mill), employing a stainless-steel container filled with steel balls of varying sizes (6.5 mm and 9.5 mm in diameter), maintaining a ball-to-powder ratio of about 10. LYC was milled in one-hour intervals for a total mill time of 3 hours, and periodically removing material adhered to the reactor walls after every interval to promote homogenous milling. The LIC blend was milled for 3 continuous hours. All preparation and milling processes were carried out under an argon atmosphere to maintain an oxygen- and moisture-free environment.

2. Electrochemical Experiments

LIC powder was hand pressed in the 6mm PEEK mold between two Ti rods to produce a semi-pelletized layer, then LYC powder was added, and hand pressed to form a bi-layer separator. A 4 mm diameter LCO electrode was interfaced with the LIC side of the separator and pressed to 380 MPa using a hydraulic press. Next, a 6mm Cu backed In foil was interfaced with the LYC side of the separator. The cell was cycled under 30 Mpa of stack pressure. The current at 1C corresponds to 140 mAg^{-1} based on the weight of cathode active material. The cells were stopped at selected SOCs and disassembled inside an Ar filled glovebox to extract the cycled LCO for ex-situ characterization. Figure S18 shows a schematic representation of the workflow.

3. Operando EDXRD analysis

Energy dispersive X-ray diffraction (EDXRD) experiments were carried out at 6-BM-A beamline of Advanced Photon Source (APS) at Argonne National Laboratory. A germanium detector was fixed at angle of $2\theta = 2.35°$ to measure the diffracted beam. The incident white beam had an energy range of 20-200keV. The X-ray beam penetrated the cell, allowing the characterization of the cell within the PEEK cell container during cycling. The EDXRD gauge had dimensions of $2 \times 4 \times 0.005$ mm^3. The detector channel number was calibrated to inverse d-spacing using a LaB_6 standard.

To prepare the cell for EDXRD analysis, LYC solid electrolyte and LCO electrode were pressed together under pressure of 300 MPa and indium foil was attached to another side of the pellet. The assembled cell

was cycled with a constant current of 0.1 C between 1.9 and 3.6V (vs Li-In alloy) under the pressure of 30 Mpa. The data acquisition time was 60 seconds. The lattice parameters of the LCO were calculated using the least square fit. The unit cell volume was calculated using UnitCell program based on the LCO lattice parameters of (003), (101), (012) and (104) reflection[41]. The unit cell volume was correlated to the amount of Li in the LCO, using a previously published study[10].

4. Nanotomography and 3D XANES analysis

Nanotomography and 3D XANES analysis were performed at the FXI beamline (18-ID) of the National Synchrotron Light Source II at the Brookhaven National Lab. For sample preparation, electrodes were carefully delaminated from the solid electrolyte pellet, configured into wedges, and sealed in a polyimide tube in Ar filled glove box. The sample was positioned on the stage for analysis, and the X-ray was directed at the tip of the wedge-shaped sample. For nanotomography, a monochromatic beam with energy of 7.725 keV was utilized to obtain clear contrast. The sample was rotated 180 degrees, with each tomographic scan lasting about one minute. The resulting spatial resolution was 20 nm. For the 3D XANES analysis, tomographic scans were carried out at each energy level, ranging from 7.588 keV to 8.153 keV over 60 steps. The spatial resolution for 3D XANES was 40 nm. For reconstructing both nanotomography and 3D XANES data, the Python-based TXM-Sandbox software was used[42,43]. Image processing and segmentation were conducted using ImageJ and AVIZO. To mitigate the influence of the surface roughness for quantifying the porosity inside the electrode, pores located within 10 μm from the current collector were reconstructed and analyzed.

5. Mechanical test

To prepare a smooth plan on the cross-section of LCO sample for nanoindentation test, focused ion beam (FIB) milling (FEI^{TM}; Versa 3D^{TM} DualBeam^{TM}) was used to polish an area of around 200*15 μm. The ion beam direction was perpendicular to the LCO surface with an accelerating voltage of 30keV. 50nA, 10nA, and 5nA ion beam currents were applied sequentially to reduce the roughness.

In-situ nanoindentation test on the FIB milled cross section was conducted with a Berkovich diamond tip inside the SEM system. The indentation positions were set in lines perpendicular to the sample's surface, with 4 points in each line at different layers (Figure 4). The point spacing in a line was 4μm, and the lines were separated by more than 10μm. Load was applied with a rate of 100 μN/s till the limit depth (400nm) was achieved. A typical load vs. displacement curve is shown in Figure S19. Several displacement bursts, or pop-in events, were observed in the curve, corresponding to cracks that developed during the nanoindentation test[44–46].

Elastic modulus and hardness of different layers were collected at an indentation depth of 50nm to avoid influence form cracks that occurred during nanoindentation. These cracks can lead to lower modulus and hardness result with increasing indentation depth[46,47]. Continuous stiffness measurement (CSM) was applied to measure the elastic modulus. Elastic modulus (E) was calculated according to Equation (2) and (3).

$$E_r = \frac{S}{2\beta}\sqrt{\frac{\pi}{A(h_c)}} \quad (2)$$

$$\frac{1}{E_r} = \frac{1-\nu^2}{E} + \frac{1-\nu_i^2}{E_i} \quad (3)$$

Here E_r was the reduced modulus that represents elastic deformation in both sample and tip. S was the dynamic material stiffness directly measured via CSM and β was a geometry constant, β=1.034 for Berkovich tip. The projected area of contact A was computed from the area function of our Berkovich tip and the calculated contact depth h_c. E_i and ν_i were Young's modulus and Poisson's ratio of the tip. For the diamond tip we used, E_i = 1070 GPa, ν_i = 0.07. Poisson's ratio of LCO was assumed to be ν = 0.3. Hardness (H) was defined as Equation 4, where P is the indentation load.

$$H = \frac{P}{A(h_c)} \quad (4)$$

The fracture toughness (K_{Ic}) can be determined via the indentation-induced pop-ins[48,49], and this pop-in method has been used to measure K_{Ic} of LCO electrodes[44,45]. Crack length c was calculated based on the displacement burst as

$$c = \sqrt{2}h_m + (Q\frac{E}{H} - \sqrt{2})h_x \quad (5)$$

Here h_m was the real displacement with pop-ins and h_x was the extra displacement caused by the entry of the tip into the crack. Definition of h_m and h_x is illustrated in Figure 1. The red dot line represents the polynomial fit of load-displacement curve before the first pop-in. The indentation load P used to determine h_m and h_x was in the range of 600-6000 μN, before the second pop-in was observed. Q is a unitless constant of 4.55 according to Field's work[49]. Fracture toughness of different layers was then calculated as

$$K_{Ic} = k(\frac{E}{H})^{\frac{1}{2}}\frac{P}{c^{3/2}} \quad (6)$$

Research has shown that the constant k mainly depends on the geometry of the indenter[48,50]. Following Jang's work[50], we estimated k = 0.028 from Equation (7), where Ψ is the half opening angle of the indenter (Berkovich tip Ψ = 65.3°).

$$k = \frac{0.0352}{(1-\nu)}(cos\Psi)^{\frac{2}{3}} \quad (7)$$

6. Computational methods

Electrochemical-transport model

The model developed includes the following mechanisms:

(a) Ion transport within the solid electrolyte separator
(b) Reaction kinetics at the LCO-solid electrolyte interface
(c) Solid-state lithium diffusion within the LCO electrode
(d) Electron transport within the LCO electrode

Ion transport within the solid electrolyte is solved based on the charge conservation equation as follows:

$$\nabla.(\kappa_{SE}\nabla\phi_{SE}) = 0 \quad (8)$$

Here, κ_{SE} and ϕ_{SE} are the ionic conductivity and electric potential for the solid electrolyte, respectively. Constant applied current is given as the boundary condition at the anode-solid electrolyte interface. Whereas

Butler-Volmer reaction kinetics is given as the boundary condition at the LCO-solid electrolyte interface as follows:

$$i_{BV} = i_o\left(exp\left(\frac{F}{2RT}(\phi_{LCO} - \phi_{SE} - U_{eq})\right) - exp\left(\frac{-F}{2RT}(\phi_{LCO} - \phi_{SE} - U_{eq})\right)\right) \quad (9)$$

Here, F is the Faraday constant, R is the universal gas constant, T is the operating temperature, U_{eq} is the equilibrium potential which is adopted from reference[51], and ϕ_{LCO} and ϕ_{SE} are the electric potentials in LCO and solid electrolyte respectively. The exchange current density, i_o, can be mathematically expressed as follows:

$$i_0 = Fk_r(c_e)^{0.5}\left(c_{s,max} - c_s\right)^{0.5}(c_s)^{0.5} \quad (10)$$

where, k_r is the reaction rate constant, c_e is the lithium-ion concentration in solid electrolyte which is assumed to be constant at 1200 mol/m^3, c_s is the local lithium concentration in LCO and $c_{s,max}$ is the maximum lithium concentration. Next, the solid-state lithium diffusion within the LCO electrode is solved using the following equation:

$$\frac{\partial c_s}{\partial t} = \nabla.(D.\nabla c_s) \quad (11)$$

where, D is the solid-state lithium diffusivity in LCO. Lastly, the electron transport within the LCO is solved based on the charge conservation equation as follows:

$$\nabla.(\sigma_{LCO}\nabla\phi_{LCO}) = 0 \quad (12)$$

Here, σ_{LCO} is the electronic conductivity of the LCO electrode.

Mechanics model

To model the stress evolution during the electrochemical operation, quasi-static mechanical equilibrium is considered for which the governing equation can be given as follows:

$$\nabla.\ \sigma = 0 \quad (13)$$

where the total strain can be mathematically expressed by the constitutive stress-strain relationship including the electrochemically induced strain:

$$\varepsilon_{ij} = \frac{1}{E}\left[(1+\upsilon)\sigma_{ij} - \upsilon\sigma_{kk}\delta_{ij}\right] + \frac{\hat{c}\Omega}{3}\delta_{ij} \quad (14)$$

Here, E is the Young's modulus, ν is the Poisson's ratio, σ_{ij} is the stress tensor, δ_{ij} denotes the Kronecker delta function, Ω is the partial molar volume and $\hat{c}$ is the difference in the lithium concentration from its reference value. All the parameters used in the modeling framework are given in Table S1.

Table S1. Parameters used in the modeling framework.

Parameters		Values	Units
R	Gas constant	8.314	J mol^{-1} K^{-1}

F	Faraday constant	96,487	C mol^{-1}
$c_{s,max}$	Maximum lithium concentration	51555[52]	mol m^{-3}
D	Solid-state diffusivity of LCO	1.5×10^{-13}	m^2 s^{-1}
k_r	Reaction rate constant	6.6×10^{-12}[51]	$m^{2.5}$ $mol^{-0.5}$ s^{-1}
κ_{SE}	Ionic conductivity of solid electrolyte	0.065	S m^{-1}
σ_{LCO}	Electronic conductivity of LCO	9.52×10^{-2}[53]	S m^{-1}
T_{ref}	Reference temperature	298	K
E_{LCO}	Young's modulus of LCO	191[54]	GPa
υ_{LCO}	Poisson's ratio of LCO	0.24[54]	-
G_{LCO}	Shear modulus of LCO	80[54]	GPa
Ω	Partial molar volume	-1.947×10^{-6}[52]	m^3 mol^{-1}

Acknowledgements

This work was supported by the Defense Advanced Research Projects Agency (DARPA) HR00112220028. This research used resources of the Advanced Photon Source, a U.S. Department of Energy (DOE) Office of Science user facility operated for the DOE Office of Science by Argonne National Laboratory under Contract No. DE-AC02-06CH11357. This research used resources 18-ID of the National Synchrotron Light Source II, a U.S. Department of Energy Office of Science User Facility operated for the DOE Office of Science by Brookhaven National Laboratory under Contract No. DE-SC0012704.

Author contributions

S.H.P. performed XANES experiments, and analyzed XANES and EDXRD characterization experiments. D. P., Y.L., P.K., and C.J.Y. assisted with EDXRD experiments. P.M. managed and oversaw modeling efforts. K.G.N. and B.V. performed meso-scale modeling. Y.W. performed nanomechanics experiments. J.R.G. oversaw nano-indention experiments and analysis. K.B.H., P.V.B. and B.Z. advised experiments and funding. K.B.H., S.H.P., and B.Z. were involved in manuscript writing. B.S, H.Y., and J.C. provided materials and engaged in discussion on analysis. J.O., A.C. and X.X. helped with experimental set-up at the synchrotron and analysis.

Competing Interests

The authors declare the following competing financial interest(s): B.S., H.Y. and J.C. are employees of Xerion Advanced Battery Corporation (XABC), and P.V.B. is a co-founder of XABC and holds an equity stake in XABC.

References

1. Zhao, Q., Stalin, S., Zhao, C. Z. & Archer, L. A. Designing solid-state electrolytes for safe, energy-dense batteries. *Nat. Rev. Mater.* **5**, 229–252 (2020).

2. Janek, J. & Zeier, W. G. Challenges in speeding up solid-state battery development. *Nat. Energy* **8**, 230–240 (2023).

3. Cui, Y. *et al.* A Fireproof, Lightweight, Polymer-Polymer Solid-State Electrolyte for Safe Lithium Batteries. *Nano Lett.* **20**, 1686–1692 (2020).

4. Jung, S. H. *et al.* Ni-Rich Layered Cathode Materials with Electrochemo-Mechanically Compliant Microstructures for All-Solid-State Li Batteries. *Adv. Energy Mater.* **10**, (2020).

5. Krauskopf, T., Richter, F. H., Zeier, W. G. & Janek, J. Physicochemical Concepts of the Lithium Metal Anode in Solid-State Batteries. *Chem. Rev.* **120**, 7745–7794 (2020).

6. Lou, S. *et al.* Insights into interfacial effect and local lithium-ion transport in polycrystalline cathodes of solid-state batteries. *Nat. Commun.* **11**, 5700 (2020).

7. Judez, X. *et al.* Opportunities for Rechargeable Solid-State Batteries Based on Li-Intercalation Cathodes. *Joule* **2**, 2208–2224 (2018).

8. Lewis, J. A. *et al.* Linking void and interphase evolution to electrochemistry in solid-state batteries using operando X-ray tomography. *Nat. Mater.* **20**, 503–510 (2021).

9. Kasemchainan, J. *et al.* Critical stripping current leads to dendrite formation on plating in lithium anode solid electrolyte cells. *Nat. Mater.* **18**, 1105–1111 (2019).

10. Naik, K. G., Vishnugopi, B. S., Datta, J., Datta, D. & Mukherjee, P. P. Electro-Chemo-Mechanical Challenges and Perspective in Lithium Metal Batteries. *Appl. Mech. Rev.* **75**, 010802 (2023).

11. Vishnugopi, B. S. *et al.* Asymmetric Contact Loss Dynamics during Plating and Stripping in Solid-State Batteries. *Adv. Energy Mater.* **13**, 2203671 (2023).

12. Koerver, R. *et al.* Chemo-mechanical expansion of lithium electrode materials-on the route to mechanically optimized all-solid-state batteries. *Energy Environ. Sci.* **11**, 2142–2158 (2018).

13. Liu, X. *et al.* Electrochemo-Mechanical Effects on Structural Integrity of Ni-Rich Cathodes with Different Microstructures in All Solid-State Batteries. *Adv. Energy Mater.* **11**, (2021).

14. Kim, U. H. *et al.* Microstructure- and Interface-Modified Ni-Rich Cathode for High-Energy-Density All-Solid-State Lithium Batteries. *ACS Energy Lett.* **8**, 809–817 (2023).

15. Besli, M. M. *et al.* Mesoscale Chemomechanical Interplay of the $LiNi_{0.8}Co_{0.15}Al_{0.05}O_2$ Cathode in Solid-State Polymer Batteries. *Chem. Mater.* **31**, 491–501 (2019).

16. Zahiri, B. *et al.* Revealing the role of the cathode–electrolyte interface on solid-state batteries. *Nat. Mater.* **20**, 1392–1400 (2021).

17. Marschilok, A. C. *et al.* Energy dispersive X-ray diffraction (EDXRD) for operando materials characterization within batteries. *Phys. Chem. Chem. Phys.* **22**, 20972–20989 (2020).

18. Shkrob, I. A., Badami, P., Okasinski, J. S., Rodrigues, M. T. F. & Abraham, D. P. Visualizing electrode assembly movement and lithiation heterogeneity in lithium-metal batteries using operando energy dispersive X-ray diffraction. *J. Power Sources* **553**, 232273 (2023).

19. Li, Z. *et al.* Synchrotron Operando Depth Profiling Studies of State-of-Charge Gradients in Thick $Li(Ni_{0.8}Mn_{0.1}Co_{0.1})O_2$ Cathode Films. *Chem. Mater.* **32**, 6358–6364 (2020).

20. Reimers, J. N. & Dahn, J. R. Electrochemical and In Situ X-Ray Diffraction Studies of Lithium Intercalation in Li_xCoO_2. *J. Electrochem. Soc.* **139**, 2091–2097 (1992).

21. Rosolen, J. M., Ballirano, P., Berrettoni, M., Decker, F. & Gregorkiewitz, M. Structural Assessment of the Electrochemical Performance Membrane Electrodes by X-Ray Diffraction and Absorption Refinements of Li_xCoO_2. *Ionics* **3**, 345–355 (1997).

22. Stavola, A. M. *et al.* Lithiation Gradients and Tortuosity Factors in Thick NMC111-Argyrodite Solid-State Cathodes. *ACS Energy Lett.* **8**, 1273–1280 (2023).

23. Bradbury, R. *et al.* Visualizing Reaction Fronts and Transport Limitations in Solid-State Li–S Batteries via Operando Neutron Imaging. *Adv. Energy Mater.* **13**, 2203426 (2023).

24. Stavola, A. M. *et al.* Lithiation Gradients and Tortuosity Factors in Thick NMC111-Argyrodite Solid-State Cathodes. *ACS Energy Lett.* **8**, 1273–1280 (2023).

25. Luo, Y. *et al.* Effect of crystallite geometries on electrochemical performance of porous intercalation electrodes by multiscale operando investigation. *Nat. Mater.* **21**, 217–227 (2022).

26. Hou, D. *et al.* Effect of the grain arrangements on the thermal stability of polycrystalline nickel-rich lithium-based battery cathodes. *Nat. Commun.* **13**, 3437 (2022).

27. Sol Kang, H. *et al.* Visualization of Nonsingular Defect Enabling Rapid Control of Structural Color. *Sci. Adv.* **8**, eabm5120 (2022).

28. Xia, H., Lu, L. & Ceder, G. Li diffusion in $LiCoO_2$ thin films prepared by pulsed laser deposition. *J. Power Sources* **159**, 1422–1427 (2006).

29. Yang, S., Yan, B., Lu, L. & Zeng, K. Grain boundary effects on Li-ion diffusion in a $Li_{1.2}Co_{0.13}Ni_{0.13}Mn_{0.54}O_2$ thin film cathode studied by scanning probe microscopy techniques. *RSC Adv.* **6**, 94000–94009 (2016).

30. Han, S., Park, J., Lu, W. & Sastry, A. M. Numerical study of grain boundary effect on Li^+ effective diffusivity and intercalation-induced stresses in Li-ion battery active materials. *J. Power Sources* **240**, 155–167 (2013).

31. Patra, A. *et al.* Electrodeposition of atmosphere-sensitive ternary sodium transition metal oxide films for sodium-based electrochemical energy storage. *Proc. Natl. Acad. Sci.* **118**, e2025044118 (2021).

32. Zhang, H. *et al.* Electroplating lithium transition metal oxides. *Sci. Adv.* **3**, e160242 (2017).

33. Gao, D., Li, Y., Lai, X., Bi, J. & Lin, D. Room-temperature synthesis of crystallized $LiCoO_2$ thin films by electrochemical technique. *J. Alloys Compd.* **509**, 697–703 (2011).

34. Zhang, X. *et al.* Assessing the roles of mechanical cracks in Ni-rich layered cathodes in the capacity decay of liquid and solid-state batteries. *Mater. Horiz.* **10**, 1856–1864 (2023).

35. Liu, D. *et al.* Towards understanding the influence of porosity on mechanical and fracture behaviour of quasi-brittle materials: experiments and modelling. *Int. J. Fract.* **205**, 57–72 (2017).

36. Jelitto, H. & Schneider, G. A. A geometric model for the fracture toughness of porous materials. *Acta. Mater.* **151**, 443–453 (2018).

37. Xu, R., Sun, H., de Vasconcelos, L. S. & Zhao, K. Mechanical and Structural Degradation of $LiNi_xMn_yCo_zO_2$ Cathode in Li-Ion Batteries: An Experimental Study. *J. Electrochem. Soc.* **164**, A3333–A3341 (2017).

38. Swallow, J. G. *et al.* Effect of Electrochemical Charging on Elastoplastic Properties and Fracture Toughness of Li_XCoO_2. *J. Electrochem. Soc.* **161**, F3084–F3090 (2014).

39. Yamakawa, S., Nagasako, N., Yamasaki, H., Koyama, T. & Asahi, R. Phase-field modeling of stress generation in polycrystalline $LiCoO_2$. *Solid State Ion* **319**, 209–217 (2018).

40. Tada, H., Paul C. Paris & George R. Irwin. The Stress Analysis of Cracks. *Del Research Corporation* **34** (1973).

41. Holland, T. J. B. & Redfern, S. A. T. UNITCELL: A nonlinear least-squares program for cell-parameter refinement implementing regression and deletion diagnostics. *J. Appl. Crystallogr.* **30**, 84 (1997).

42. Xiao, X., Xu, Z., Lin, F. & Lee, W.-K. *TXM-Sandbox* : an open-source software for transmission X-ray microscopy data analysis. *J. Synchrotron. Radiat.* **29**, 266–275 (2022).

43. Xiao, X., Xu, Z., Hou, D., Yang, Z. & Lin, F. Rigid registration algorithm based on the minimization of the total variation of the difference map. *J. Synchrotron. Radiat.* **29**, 1085–1094 (2022).

44. Qu, M. *et al.* Nanomechanical quantification of elastic, plastic, and fracture properties of $LiCoO_2$. *Adv. Energy Mater.* **2**, 940–944 (2012).

45. Swallow, J. G. *et al.* Effect of Electrochemical Charging on Elastoplastic Properties and Fracture Toughness of Li_XCoO_2. *J. Electrochem. Soc.* **161**, F3084–F3090 (2014).

46. Cheng, E. J., Taylor, N. J., Wolfenstine, J. & Sakamoto, J. Elastic properties of lithium cobalt oxide ($LiCoO_2$). *J. Asian Ceram. Soc.* **5**, 113–117 (2017).

47. Xu, R., Sun, H., de Vasconcelos, L. S. & Zhao, K. Mechanical and Structural Degradation of $LiNi_xMn_yCo_zO_2$ Cathode in Li-Ion Batteries: An Experimental Study. *J. Electrochem. Soc.* **164**, A3333–A3341 (2017).

48. Pharr, G. M., Harding, D. S. & Oliver, W. C. Measurement of Fracture Toughness in Thin Films and Small Volumes Using Nanoindentation Methods. *Mechanical Properties and Deformation Behavior of Materials Having Ultra-Fine Microstructures* 449–461 (1993).

49. Field, J. S., Swain, M. V. & Dukino, R. D. Determination of fracture toughness from the extra penetration produced by indentation-induced pop-in. *J. Mater. Res.* **18**, 1412–1419 (2003).

50. Jang, J. & Pharr, G. M. Influence of indenter angle on cracking in Si and Ge during nanoindentation. *Acta. Mater.* **56**, 4458–4469 (2008).

51. Barai, P. *et al.* Investigation of Delamination-Induced Performance Decay at the Cathode/LLZO Interface. *Chem. Mater.* **33**, 5527–5541 (2021).

52. Wu, L., Wen, Y. & Zhang, J. Three-Dimensional Finite Element Study on Li Diffusion Induced Stress in FIB-SEM Reconstructed $LiCoO_2$ Half Cell. *Electrochim. Acta* **222**, 814–820 (2016).

53. Johnson, A. C. *et al.* Strategies for approaching one hundred percent dense lithium-ion battery cathodes. *J. Power Sources* **532**, 231359 (2022).

54. Cheng, E. J., Taylor, N. J., Wolfenstine, J. & Sakamoto, J. Elastic properties of lithium cobalt oxide ($LiCoO_2$). *J. Asian Ceram. Soc.* **5**, 113–117 (2017).

Supporting information

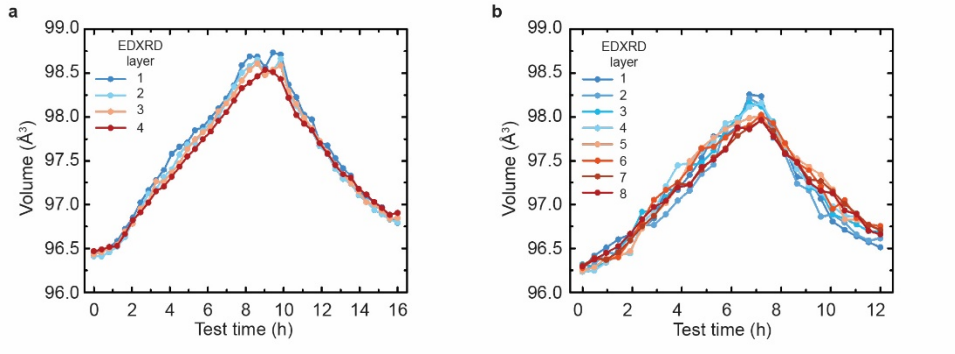

Figure S1. Variation of unit cell volume for (**a**) 1 and (**b**) 3 mAh cm^{-2} LCO.

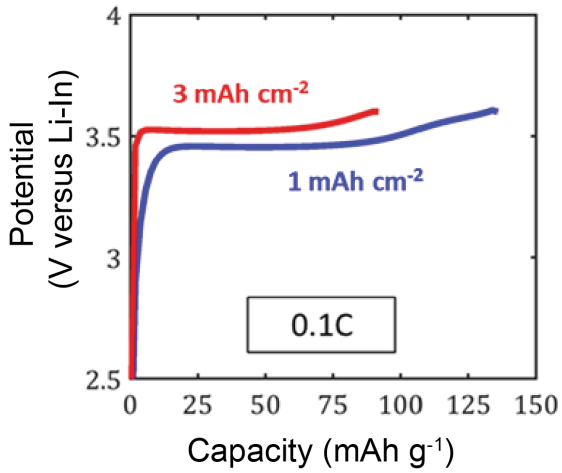

Figure S2. Modeled voltage profile for a charging of 1 and 3 mAh cm^{-2} LCO.

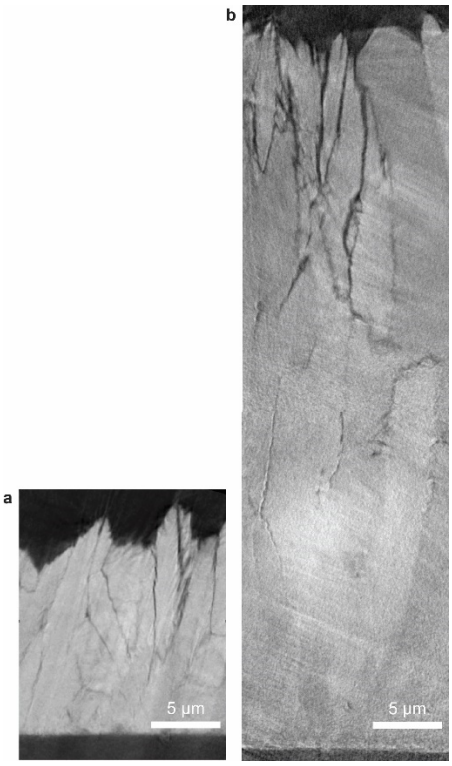

Figure S3. Reconstructed 2D image slices of LCO electrode for (**a**) 1 and (**b**) 3 mAh cm^{-2} LCO. Image slices were used for Li diffusion modeling.

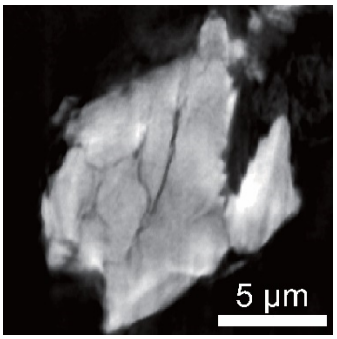

Figure S4. Reconstructed 2D image slices of LCO powder delaminated from the charged 1 mAh cm^{-2} LCO. The image corresponds to 3D XANES slice 2 in Figure 2h.

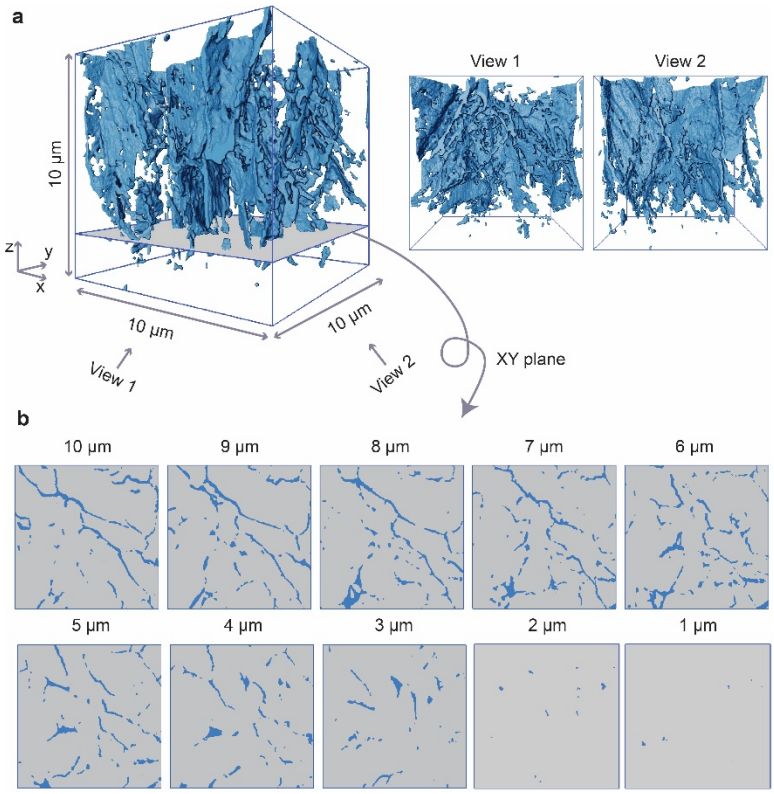

Figure S5. **a**, Reconstructed 3D image of pores in the pristine LCO displayed in Figure 3c with various perspectives views. **b**, Corresponding XY planes with different distances from the current collector.

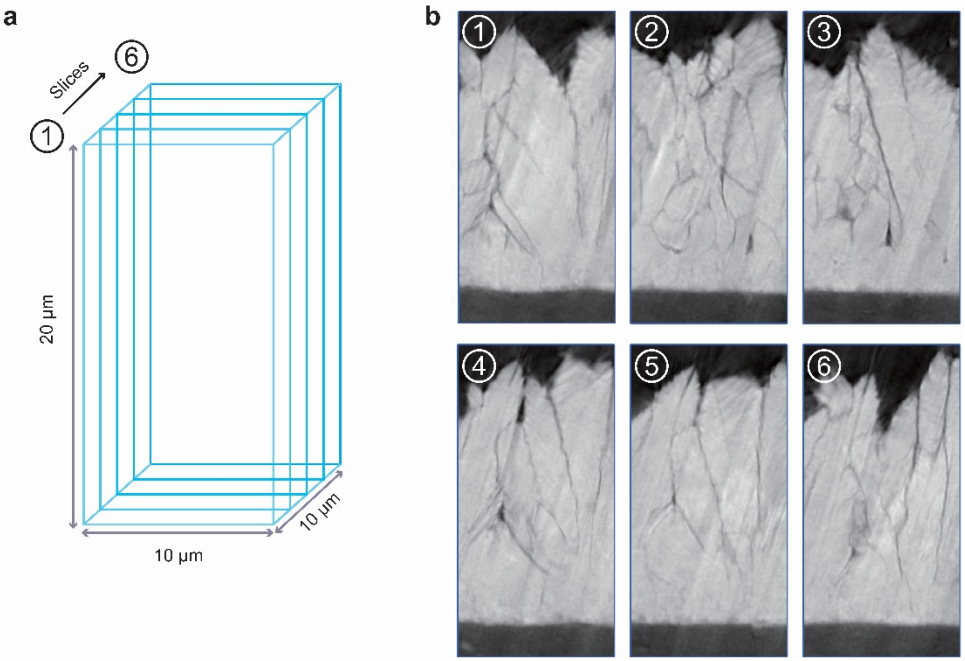

Figure S6. **a**, Schematic illustration of image slice locations. **b**, Reconstructed 2D image slices of the pristine LCO. Each slice apart each other for 2 µm.

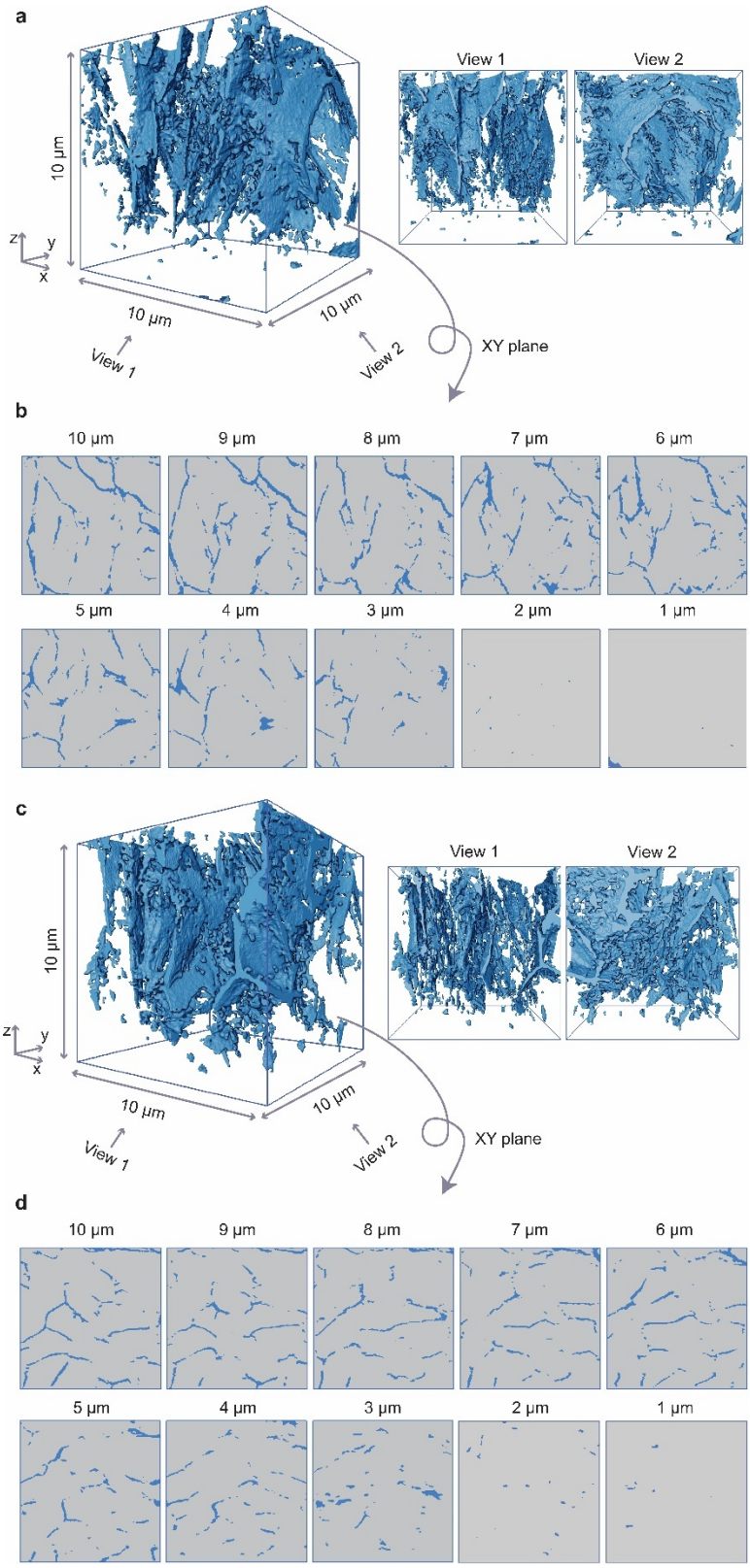

Figure S7. **a**,**c**, Reconstructed 3D image of pores in the pristine LCO at different locations. **b**,**d**, Corresponding XY planes with different distances from the current collector.

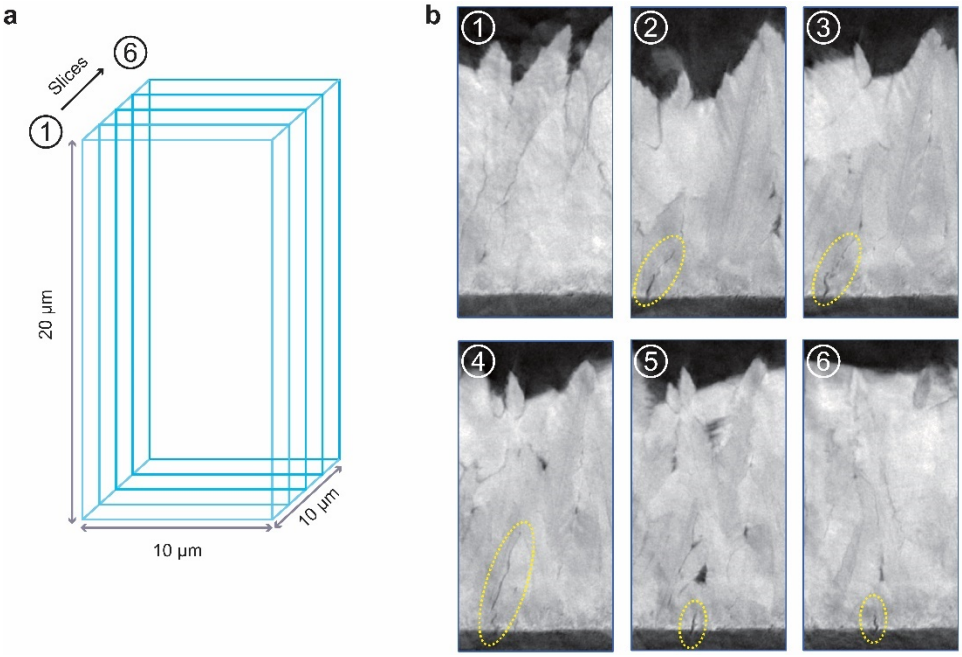

Figure S8. **a**, Schematic illustration of image slice locations. **b**, Reconstructed 2D image slices of the LCO charged to 3.6 V. Each slice apart each other for 2 µm. Pores formed at the current collector side are marked as dashed yellow circle.

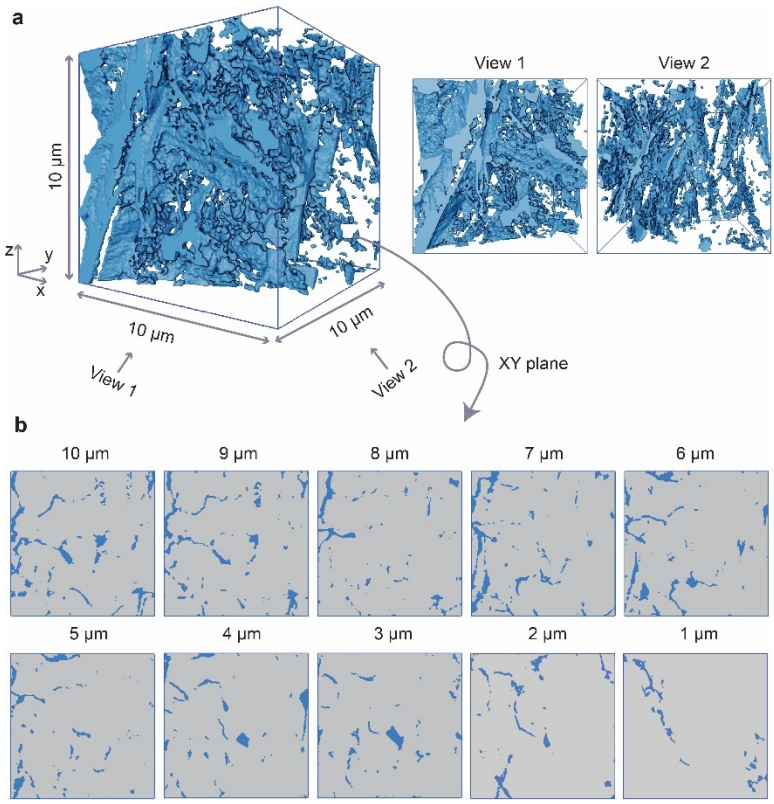

Figure S9. **a**, Reconstructed 3D image of pores in the charged LCO displayed in Figure 3e with various perspectives views. **b**, Corresponding XY planes with different distances from the current collector.

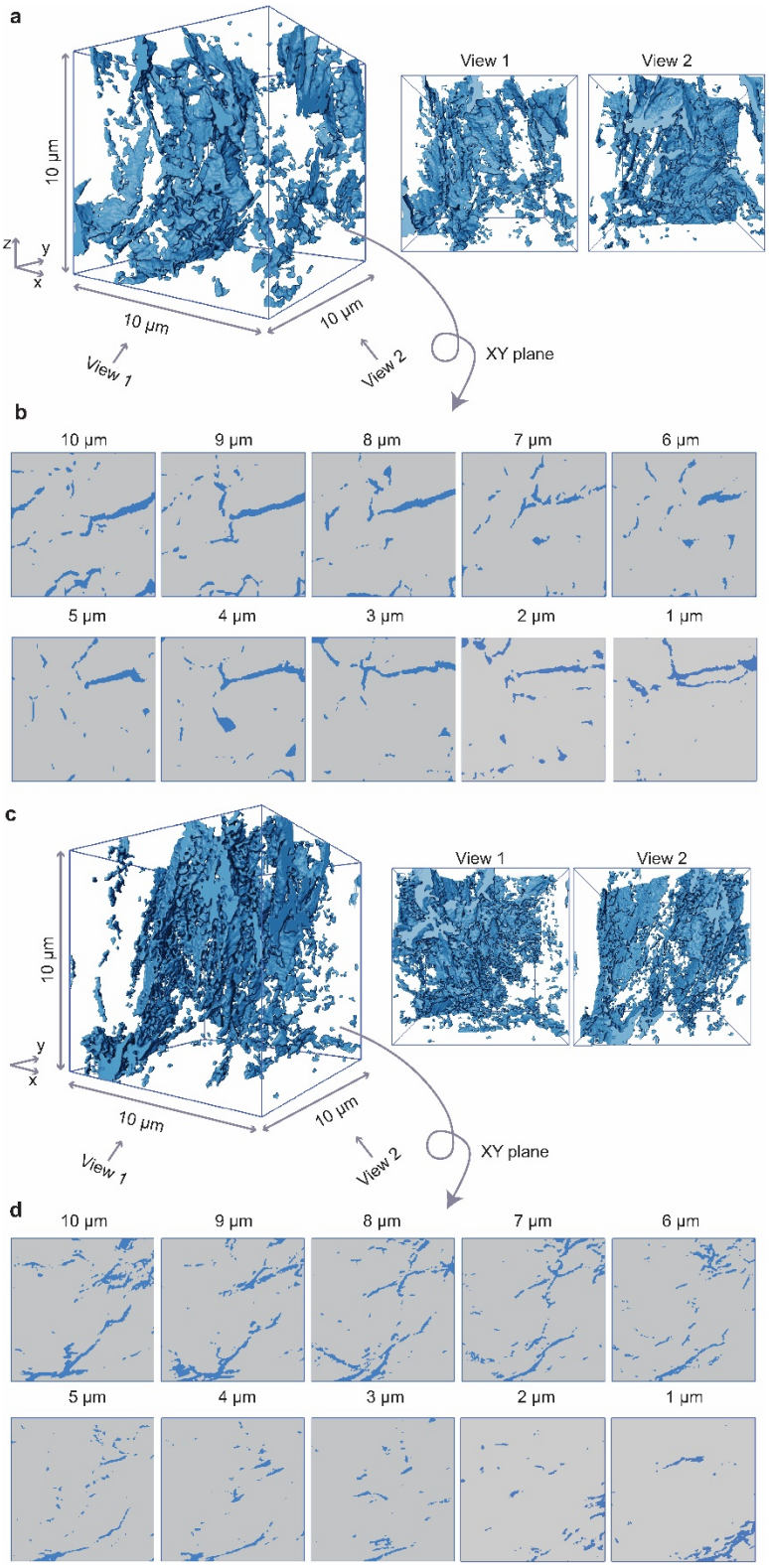

Figure S10. **a**,**c**, Reconstructed 3D image of pores in the charged LCO at different locations. **b**,**d**, Corresponding XY planes with different distances from the current collector.

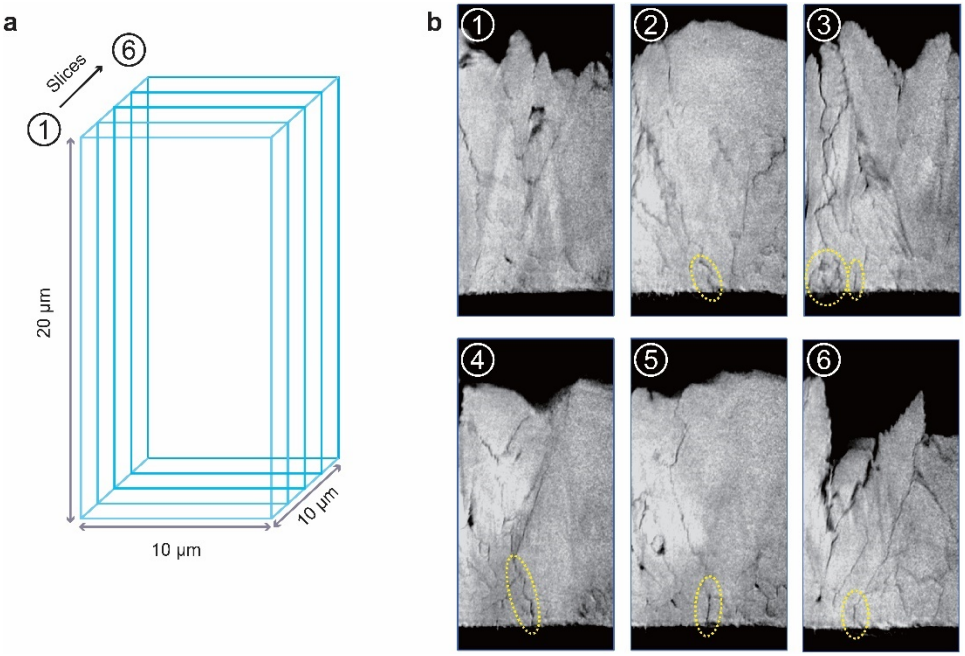

Figure S11. **a**, Schematic illustration of image slice locations. **b**, Reconstructed 2D image slices of the LCO discharged to 1.9 V. Each slice apart each other for 2 µm. Pores formed at the current collector side are marked as dashed yellow circle.

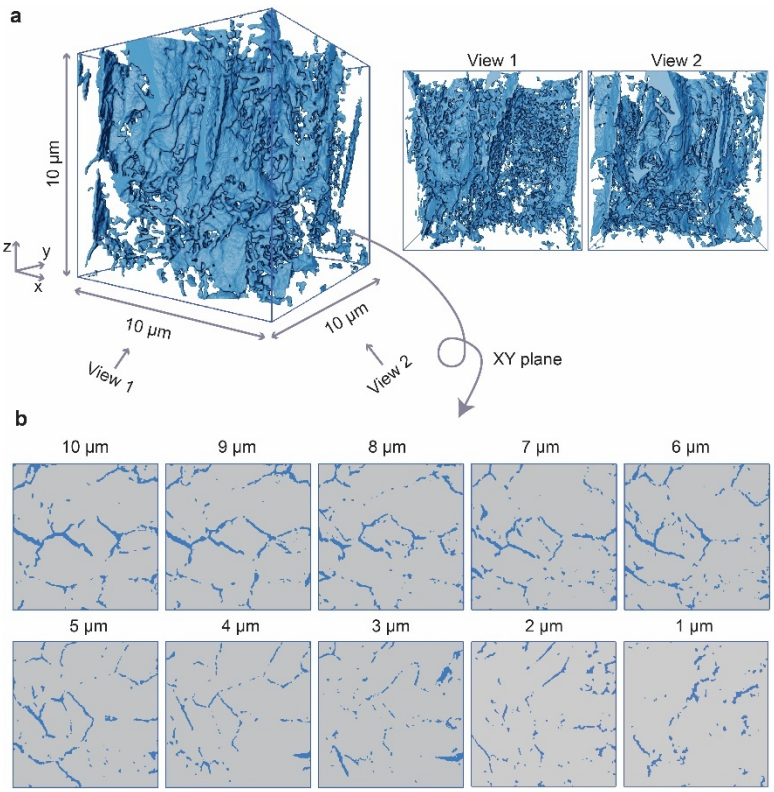

Figure S12. **a**, Reconstructed 3D image of pores in the discharged LCO displayed in Figure 3g with various perspectives views. **b**, Corresponding XY planes with different distances from the current collector.

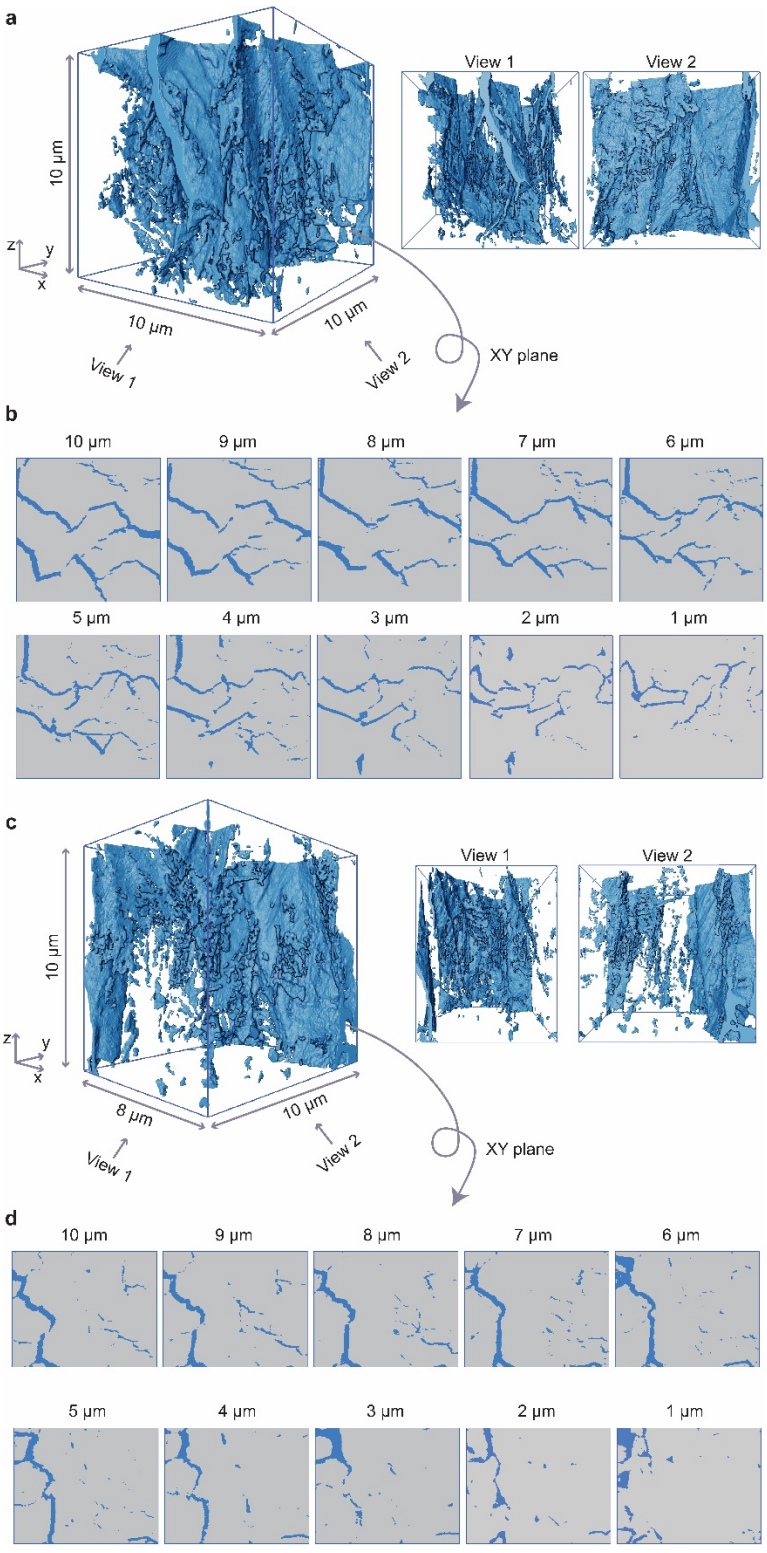

Figure S13. **a**,**c**, Reconstructed 3D image of pores in the discharged LCO at different locations. **b**,**d**, Corresponding XY planes with different distances from the current collector.

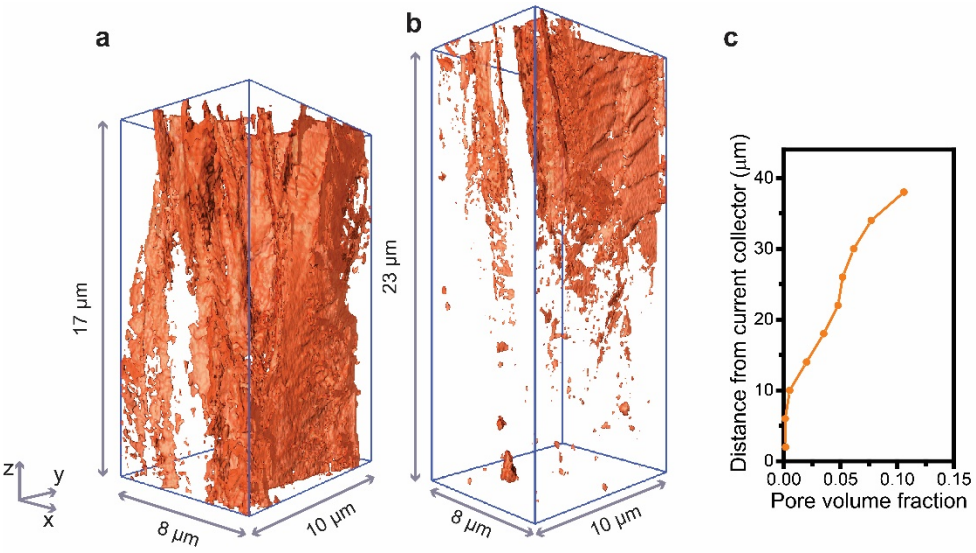

Figure S14. a, b, Reconstructed 3D image of pores in the 3 mAh cm^{-2} LCO electrode. Since the thickness of 3 mAh cm^{-2} LCO electrode is larger than observation range of analysis, the electrode was observed by taking tomogram in two regions. **a** for solid electrolyte side and **b** for current collector side. **c**, Porosity variation along the z-axis in LCO electrode.

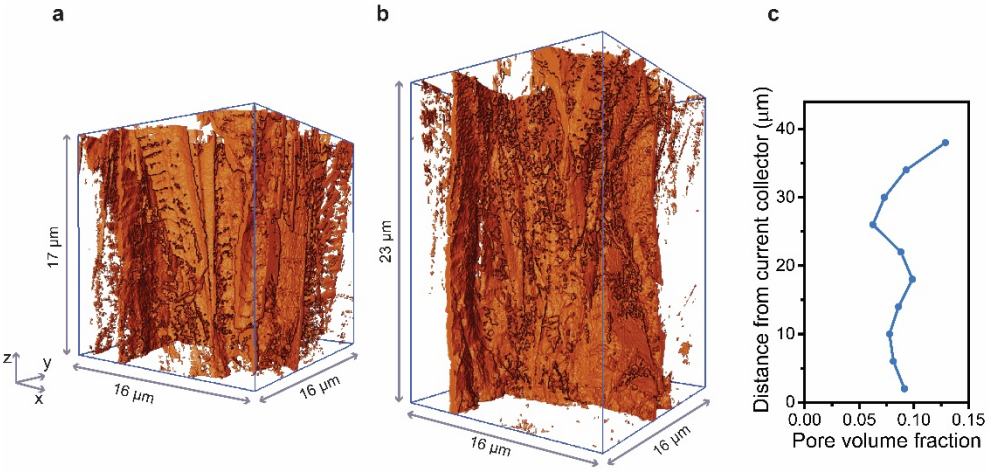

Figure S15. a, b, Reconstructed 3D image of pores in the 3 mAh cm^{-2} LCO electrode after charging. **a** for solid electrolyte side and **b** for current collector side. **c**, Porosity variation along the z-axis in LCO electrode.

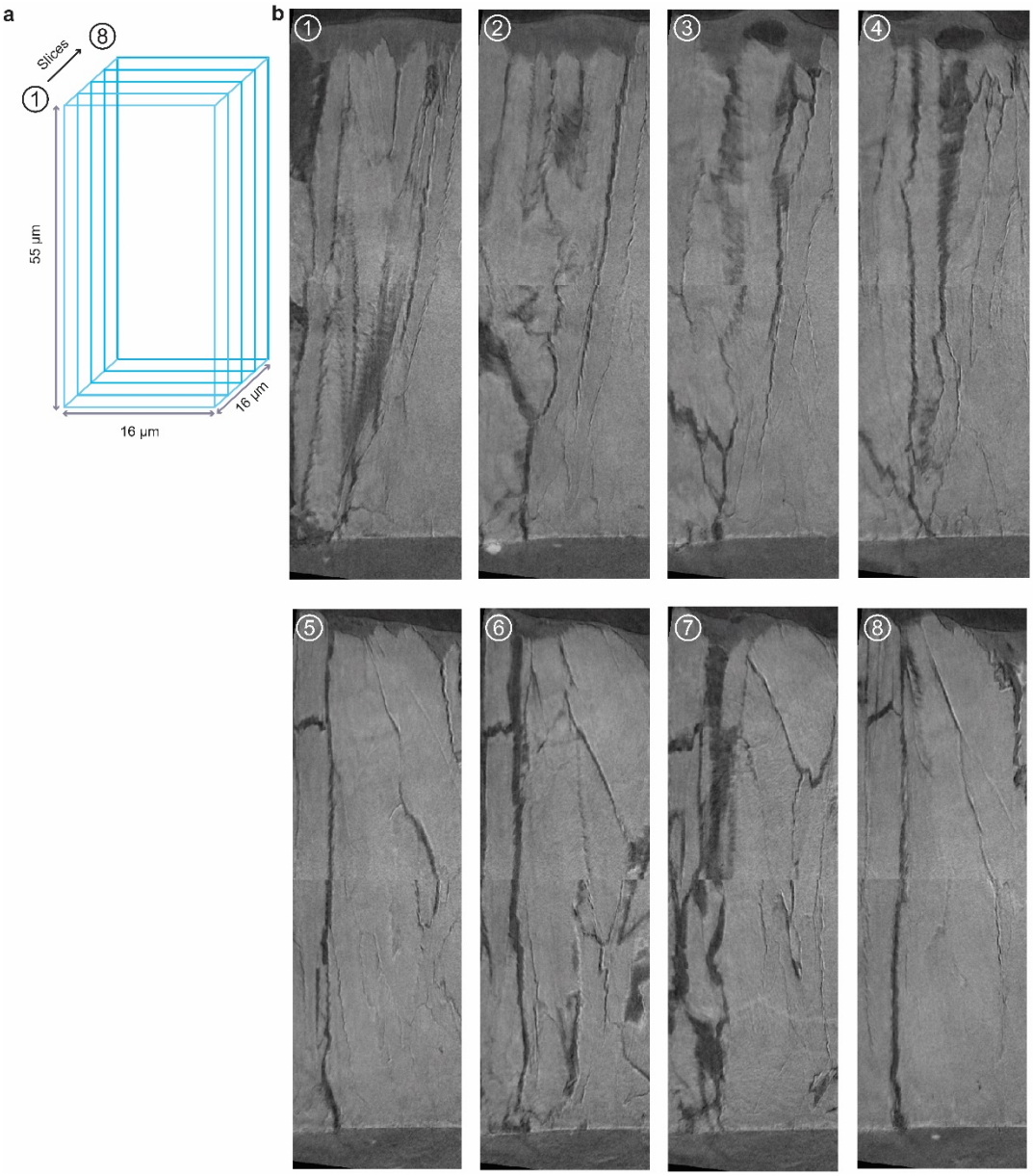

Figure S16. **a**, Schematic illustration of image slice locations. **b**, Reconstructed 2D image slices of the 3 mAh cm^{-2} LCO charged to 3.6 V. Each slice apart each other for 2 µm.

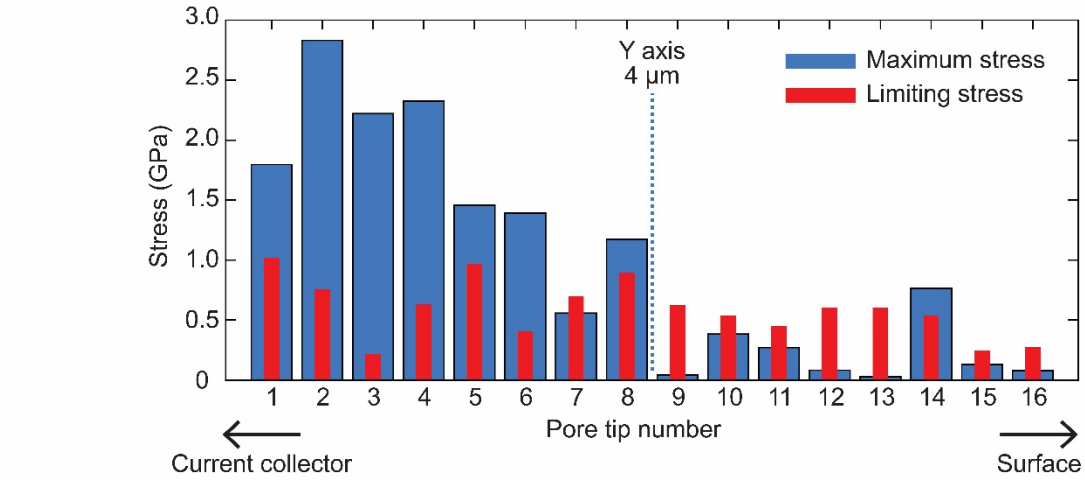

Figure S17. Comparison of the maximum stress applied at each pore tip and corresponding limiting stress calculated based on the fracture toughness of charged electrode.

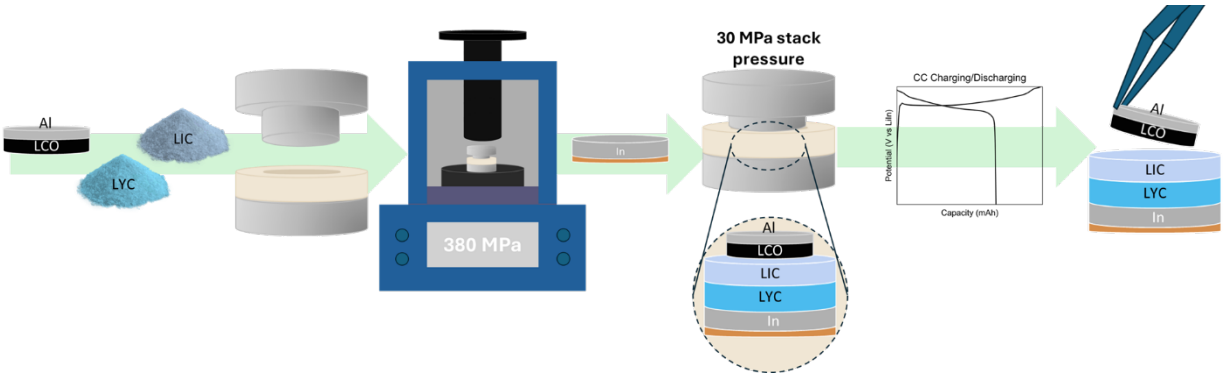

Figure S18. Schematic representation of workflow for *ex-situ* nanotomography analysis sample preparation.

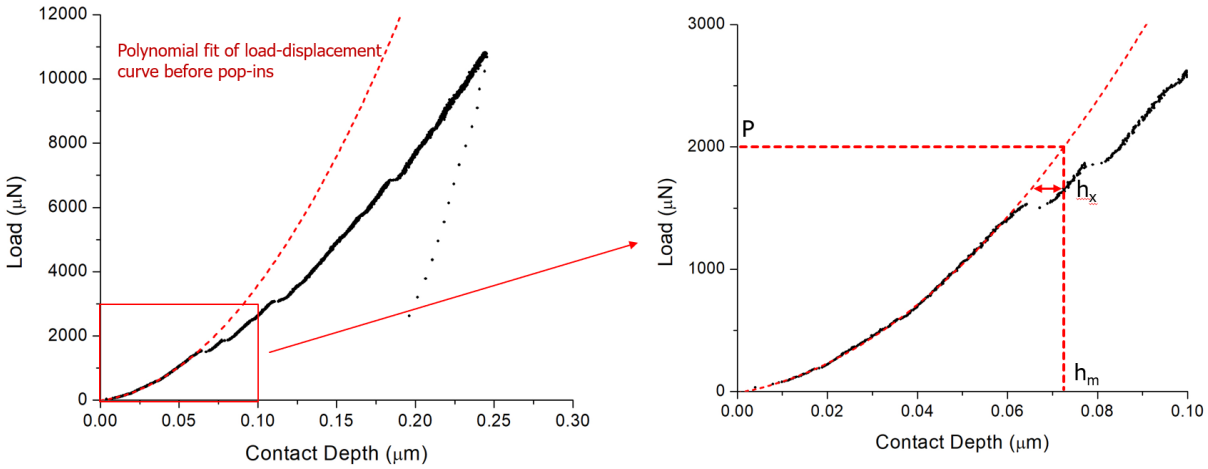

Figure S19. a. Typical load-displacement data of nanoindentation test on LCO cross-section, with pop-ins corresponding with cracks. Red dot line stands for the polynomial fitting before the first pop-in. **b.** Definition of the real displacement with pop-ins h_m and the extra displacement caused by the crack h_x.